Crystal Structure and Stability of Phases in Mg-Zn Alloys: A Comprehensive First-Principles Study

Du Cheng, Kang Wang*, Bi-Cheng Zhou*

Department of Materials Science and Engineering, University of Virginia, Charlottesville, VA 22904

Abstract

Mg-Zn alloys form the basis of a wide variety of commercial light-weight Mg alloys due to their precipitation hardenability, biocompatibility, and low cost. Despite significant progress, there exist controversies over the crystal structures and stabilities of various complex precipitates in this important binary system. In this work, the information about crystal structures and stabilities of phases in Mg-Zn system is critically reviewed and three key open questions are identified: (1) What are crystal structures of Guinier-Preston (GP) zones? (2) What are relative stabilities of a myriad of phases observed for β'_1 precipitates? (3) Why does the β'_2 phase have two distinct orientation relationships (ORs)? To shed light on these questions, comprehensive first-principles calculations based on density functional theory, cluster expansion, and Monte Carlo simulations are performed. The atomic structures of GP zones are predicted, and the effect of coherency strain on their stabilities are analyzed. The structures of β'_1 precipitates composed of the rhombic MgZn₂ and the elongated hexagonal Mg₆Zn₇ units are provided. It is shown that the β'_1 precipitate can be stabilized with increased fraction of rhombic MgZn₂ units, which leads to local regions of the C14 MgZn₂ Laves phase. The origin of the two distinct ORs between β'_2 phase and the matrix is traced back to two formation paths, i.e., relaxation of the coherent Zn ordering on HCP matrix and coarsening of C14 MgZn₂ region in β'_1 precipitates. Finally, a feasible precipitation sequence in Mg-Zn alloys is suggested.

Keywords: Mg-Zn alloys, precipitates, phase stability, first-principles.

Corresponding author: Kang Wang (<u>kw7rr@virginia.edu</u>), Bi-Cheng Zhou (<u>bicheng.zhou@virginia.edu</u>)

1. Introduction

Mg alloys, as the lightest structural metallic materials, have been studied extensively for their wide potential applications in aerospace and automotive industries, where weight is a crucial factor to reduce the energy cost and CO₂ emission [1-3]. Among Mg-based alloys, Mg-Zn alloys received tremendous attention due to its precipitation strengthening capability [3], biocompatibility [4,5] and low cost [6]. The maximum solubility of Zn in Mg matrix is 2.4 at.% at 613 K (340 °C) [3], which decreases rapidly with lowering temperature and leads to supersaturated solid solution (S.S.S.S.) [7]. Aging treatment of S.S.S.S. leads to formation of various precipitates that impede the movement of dislocations and improves the strength of the alloy. Biochemically, Mg and Zn species can be absorbed by human body and bivalent ions of Mg and Zn are essential for human metabolism [8,9]. If the absorption rate is properly tuned, Mg-Zn alloys could become a promising candidate for various implants (e.g., bone screws, cardiovascular stent) [9,10]. As for availability, elemental Mg and Zn are abundant and inexpensive compared with rare earth (RE) elements commonly used in Mg alloys [1,6]. Mg-Zn system is also a critical subsystem for commercial Mg alloys, e.g., AZ series (Mg-Al-Zn alloys), ZK series (Mg-Zn-Zr alloys) and ZE series (Mg-Zn-RE alloys) [11] due to Zn's ability to form precipitates with a larger atom in Mg matrix.

Over the years, numerous efforts have been made to understand and tune the microstructures of Mg-Zn alloys since the discovery of its age hardening effect [3,5,20–26,12–19]. Although remarkable progress has been made, the structures and stabilities of the phases in Mg-Zn system are still not well understood. Specifically, there are considerable debates on the exact stoichiometry and details of the atomic structure of the metastable phases in the Mg-Zn system, especially the precipitates in the early stages of aging treatment [3]. In the current work, we review the current knowledge on the phases in Mg-Zn system and identify three key open questions on phase structure and stability (Section 2.3). Then, comprehensive first-principles calculations based on density functional theory (DFT)[27,28], cluster expansion (CE) [29] and Monte Carlo (MC) [30] are performed to fill the knowledge gap and answer these questions from computational perspectives. The computational methodology is detailed in Sec. 3. The results are discussed, including the overall phase structures and stabilities (Sec. 4.1), potential GP zones (Sec. 4.2), effect of lattice mismatch (Sec. 4.3) and formation of incoherent precipitates (Sec. 4.4). Finally, a precipitation

sequence is proposed by summarizing the experimental information in the literature and insights from current calculations (Sec. 4.4).

2. Literature review

The crystallography of phases and their microstructures in Mg-Zn alloys during processing often display a rich variety of complexity. In this Section, a critical review on the research status is given on the intermetallic compounds and precipitates in Mg-Zn alloys. The categorization of structures into intermetallic compounds and precipitates is due to the terminologies in different research communities (e.g., crystallography and metallurgy), despite the overlapping of concepts. The intermetallic compounds are reviewed in Sec. 2.1 focusing on the crystallographic aspect, while the review on precipitations focuses on the microstructures in aging process. The phase diagram of Mg-Zn system by Okamoto is shown in Fig. 1 for an overview of the phase relation [7].

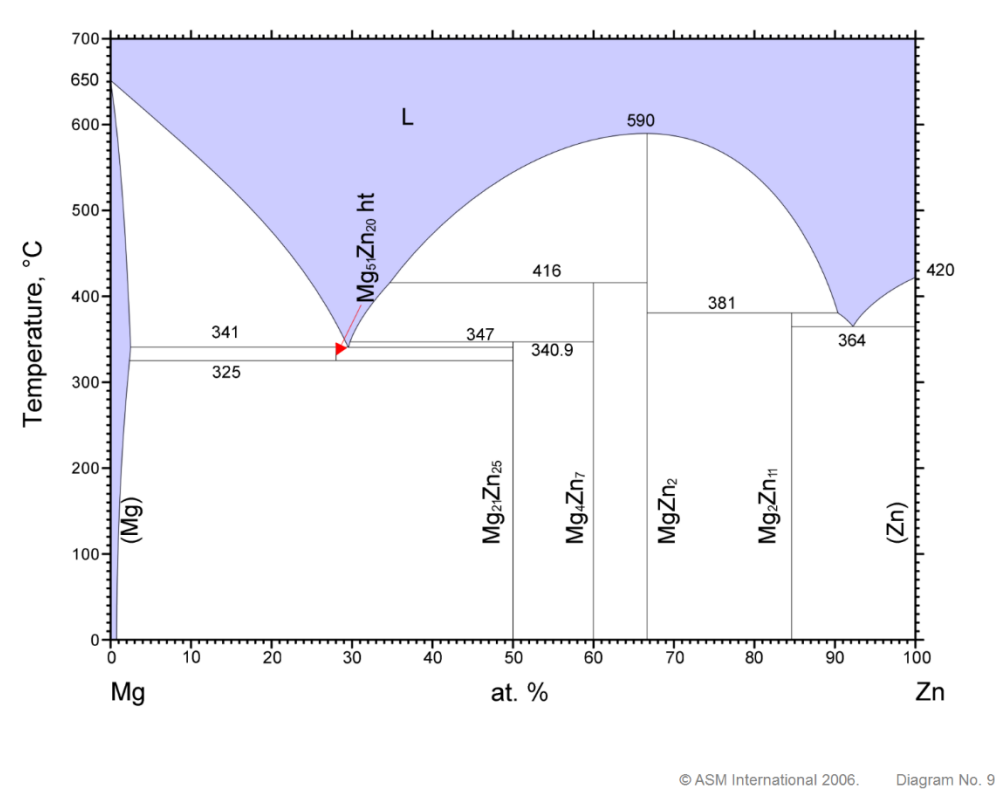


Fig. 1 Phase diagram of Mg-Zn system [7], retrieved from the ASM Alloy Phase Diagram Database.

2.1 Intermetallic compounds

$2.1.1 \text{ Mg}_{51}\text{Zn}_{20} (\text{Mg}_{7}\text{Zn}_{3})$

Mg₅₁Zn₂₀ (or conventionally known as Mg₇Zn₃) is the compound with the lowest Zn concentration, i.e., ~ 30 at.% Zn, among all the binary intermetallic compounds. It is stable within temperature range of 325 to 341 °C according to the experimental Mg-Zn phase diagram shown in Fig. 1 [7]. The crystal structure of Mg₅₁Zn₂₀ (Immm, a = 14.083 Å, b = 14.486 Å and c = 14.025 Å) was first reported by Higashi et al. based on single-crystal X-ray diffraction (XRD) [31]. The structure can be described as an arrangement of icosahedral polyhedra, which is basically the same as those of Mackay icosahedron (MI)-type quasicrystal approximant [31,32]. This atomic structure is later confirmed by transmission electron microscopy (TEM)in binary Mg-Zn alloys by Gao et al. [33] and Nemec et al. [23].

$2.1.2 \text{ Mg}_{21}\text{Zn}_{25} (\text{MgZn})$

Mg₂₁Zn₂₅ (or conventionally known as MgZn) is the compound with Zn concentration slightly larger than 50 at.%. Since a large fraction of Mg₂₁Zn₂₅ or MgZn is usually observed in this binary alloy after equilibration, this phase is usually denoted as the equilibrium β phase. The conventionally designated MgZn phase was originally suggested by Hume-Rothery et al.[23], and later different crystal structures was proposed for MgZn, including the hexagonal crystal structure by Tarschisch [34], the orthorhombic structure McKeehan et al. [35], the rhombohedral structure by Khan [36], a base-centered monoclinic structure by Gao et al. based on TEM [33]. A slightly different stoichiometry of Mg₁₂Zn₁₃ was also suggested for this phase by Clark et al. using XRD [23,37], but the structural information was not reported.

The stoichiometry of $Mg_{21}Zn_{25}$ is accepted in recent publications [23,35,38]. Its crystal structure ($R\bar{3}c$, $a=b=25.7758\,\text{Å}$, $c=8.7624\,\text{Å}$, $\alpha=\beta=90^\circ$ and $\gamma=120^\circ$) was first proposed by Cerny et al. based on XRD [35] and further confirmed by other TEM and high angle annular dark field scanning transmission electron microscopy (HAADF-STEM) investigations [23,38,39]. This complex crystal structure has C14 Laves-type hexagonal columns isolated by the Mg-rich transition region with an orientation relationship of $[11\bar{2}0]_{C14} \parallel [1\bar{1}00]_{Mg_{21}Zn_{25}}$ and $[10\bar{1}0]_{C14} \parallel [11\bar{2}0]_{Mg_{21}Zn_{25}}$, respectively [35,40]. Further observation shows that C14 Laves-type columns can overlap with each other due to the local enrichment of Zn, leading to nanometer-sized C14 domains within $Mg_{21}Zn_{25}$ phase [38].

$2.1.3 \text{ Mg}_4\text{Zn}_7 (\text{Mg}_2\text{Zn}_3)$

Mg₄Zn₇ (or conventionally known as Mg₂Zn₃) is the compound with Zn concentration of 60~63.6 at.%. This phase is first suggested to have a composition of Mg₂Zn₃ with a triclinic structure by Gallot and Graf [3,41]. But this crystal structure has not been experimentally confirmed. Later, it is proposed that this phase has a stoichiometry of Mg₄Zn₇ with a base-centered monoclinic structure (B/2m, a = 25.96 Å, b = 14.28 Å, c = 5.24 Å, $\gamma = 102.5^{\circ}$) [42]. Using TEM, Gao and Nie confirmed this structure and reported the orientation relationship of $[001]_{\text{Mg}_4\text{Zn}_7} \sim \|[0001]_{\alpha} \text{ and } (630)_{\text{Mg}_4\text{Zn}_7} \sim \|(01\overline{1}0)_{\alpha} \text{ with Mg matrix [33]}.$

The Mg₄Zn₇ phase resembles the Frank-Kasper phase (a common type of the topologically close packed phase) and is closely related to 2D icosahedral quasicrystal [43]. Viewed along [010] direction, the Mg₄Zn₇ phase is characterized by the MgZn₂ rhombic units and the Mg₆Zn₇ elongated hexagonal units. The MgZn₂ rhombic unit is the same with the building unit of C14 and C15 MgZn₂ Laves phases. The Mg₆Zn₇ elongated hexagonal unit can be formed by one rectangle unit and two icosahedral chains outside the rectangle [44]. In other words, the Mg₄Zn₇ phase is a Frank-Kasper type decagonal 2D quasicrystal approximant with a relative small unit cell compared with most approximants [45]. Similar decagonal quasicrystal and approximants built by hexagonal and rhombic units are reported in Mg-Zn-RE system [46–48].

2.1.4 C14 and C15 Laves phase MgZn₂

There are two phases that have stoichiometry of MgZn₂, i.e., C14 and C15, and there is no controversy about their composition. The C14 MgZn₂ is stable up to 590 °C in Mg-Zn phase diagram in Fig. 1 [7]. Its crystal structure was first discovered by Friauf in 1927 [49]. Later, Laves and his coworkers performed extensive research on C14 MgZn₂, which is thus named Laves phase [50–52]. The C14 MgZn₂ has a hexagonal structure (P6₃/mmc, a = 5.221 Å, c = 8.57 Å) [53]. Viewed along [2 $\overline{110}$] direction, it is identified as zigzag-stacked MgZn₂ rhombic units packed along [0001] direction. Recently, in the exploration of intermediate phases in Mg-Zn alloys, metastable MgZn₂ with C15 structure is also found [54,55]. C15 MgZn₂ has a face centered cubic structure (Fd $\overline{3}$ m, a = b = c = 5.234 Å) [56] built by the same rhombic units in C14 MgZn₂ but stacked in an aligned pattern along [001] direction [54,55]. Both C14 and C15 Laves MgZn₂ belong to the Frank-Kasper phases, which are structurally related to a large number of quasicrystals and their approximants [45,52]. Icosahedral clusters, i.e., the unit structure of quasicrystal, can be found within C14 and C15 Laves MgZn₂ [57,58]

2.1.5 Mg₂Zn₁₁

There is no controversy involving the stoichiometry of Mg_2Zn_{11} phase. The structure of Mg_2Zn_{11} (Pm $\overline{3}$, a = b = c = 8.54 Å) is first determined by Samson based on single-crystal XRD study [59]. This structure can be seen as a cubic packing of Pauling triacontahedra linked through Zn octahedral or as an embedding of icosahedra in an FCC matrix, which is structurally related with the simple C14 Laves $MgZn_2$ phase, the quasicrystals and approximants typically in ZnMgAl and Zn(Mg)Sc systems [60].

2.2 Precipitates

2.2.1 Precipitation sequence

The precipitation sequence in Mg-Zn alloys depends on the alloy composition and thermal history. Using early TEM, Clark reported that the precipitation sequence in Mg-5wt.%Zn alloy follows S.S.S.S. \rightarrow MgZn' (rod-like coherent C14 Laves phase MgZn₂) \rightarrow MgZn at the temperature of 149 °C and above [12]. Based on XRD analysis and electron microscopy, Mima et al. suggested that in Mg-4wt. %Zn alloy the precipitation sequence is S.S.S.S. \rightarrow pre- $\beta' \rightarrow \beta' \rightarrow \beta$ (MgZn) for temperature above 110 °C and S.S.S.S. \rightarrow GP zone \rightarrow pre- $\beta' \rightarrow \beta'$ for temperature ranging from 60 to 110 °C [16]. In the early literatures, MgZn' and β' refers to the rod-like precipitates, corresponding to β'_1 in recent publications, while pre- β' refers to the preliminary precipitates that were observed before β' . Based on Laue XRD, Takahashi et al. suggested that the precipitation sequence is S.S.S.S. \rightarrow GP 1 zones \rightarrow GP 2 zones \rightarrow $\beta_1' \rightarrow$ $\beta_2' \rightarrow$ β [17]. Using TEM, Wei et al. reported the transition from rod-like β'_1 to disc-like β'_2 is the onset of over aging [18]. In recent publications, the commonly accepted precipitation sequence is S.S.S.S. \rightarrow GP zones \rightarrow $\beta_1' \rightarrow$ $\beta_2' \rightarrow$ β [3,21]. The structures of GP zones, β_1' and β_2' are discussed in the following sections.

2.2.2 GP zones

The GP zones in Mg-Zn system are usually described as coherent nano-scale precipitates of a few atomic layers on certain crystalline planes of Mg matrix. In 1962, Murakami employed Laue XRD and showed the formation of GP zones that causes age hardening is on the $\{10\overline{1}0\}$ plane at the temperature range of 70-100 °C [61]. In 1969, Mima et al. suggested existence of GP zone from the difference in thermal behavior compared with pre- β' in Mg-4 wt.% Zn specimen during aging process, in spite of the lack of direct evidence from electron microscopy [16]. Using Laue

XRD, Takahashi et al. discovered patterns for GP 1 and GP 2 zones, where GP 1 is plate-like on $\{11\bar{2}0\}$ plane formed below 60 °C and GP 2 oblate spheroid on basal plane that forms below 80 °C [17]. Komatsu et al. also suggested the existence of GP zones in Mg-4wt.%Zn alloy due the increase in electrical resistivity at temperatures up to 333 K (60°C) [19]. Direct observation of GP zones is challenging due to its small size and coherency with the matrix. With modern high resolution TEM, Buha observed Zn clusters and GP zones on $\{0001\}_{\alpha}$ and $\{2\overline{110}\}_{\alpha}$ planes in Mg-2.8 at.% Zn alloys heat treated at 70-100 °C [21]. However, the experimental evidence is considered insufficient to support the existence of such Zn clusters and GP zones [3]. The increased hardness attributed to GP zones in this work are also unrealistically high compared with those reported by the others [3]. In Mg-2.4 at.% Zn alloys aged at 70 °C for 100 h, Bhattacharjee et al. reported the formation of GP zone from 3 dimensional atom probe (3DAP) result, and suggested early stage GP zones serve as heterogeneous nuclei for the β'_1 [62]. Zhou et al. reported observation of GP zones on $\{0001\}_{\alpha}$ and $\{2\overline{1}\overline{1}0\}_{\alpha}$ planes in TEM results in Mg-4 wt.% Zn alloys processed by high strain rate rolling, pre-aging at 70°C and aging at 160°C [5], although the detailed atomic structures are not reported. In the Mg-5.78Zn-0.44Zr wt.% alloy processed by integrated extrusion and equal channel angular pressing at 623K (350°C) and then aging at room temperature, GP zones on $\{10\overline{1}0\}_{\alpha}$ plane were reported in their HAADF STEM images [63]. It is accepted that Zr plays the role of grain refiner and does not change the atomic structures of binary Mg-Zn precipitates [64,65]. So far, many experimental studies suggested the existence of GP zones in Mg-Zn alloys, although direct imaging that can definitively resolve the issue is still lacking.

2.2.3 β'_1 precipitates

The metastable precipitate that forms after GP zones is named β_1' , which usually has a rod-like morphology perpendicular to the basal plane of Mg matrix and appear in the peak-aged samples. There has been controversy for the crystal structure of β_1' precipitates. In early literatures of precipitation in Mg-Zn alloys, β_1' precipitates, also described as MgZn' or β' [12,66], were determined from XRD and selected-area electron diffraction (SAED) to have the same structure with C14 Laves phase MgZn₂ with an orientation relationship of $[0001]_{C14} \parallel [11\bar{2}0]_{Mg}$ and $(11\bar{2}0)_{C14} \parallel (0001)_{Mg}$ with the Mg matrix [18,66]. Another hexagonal structure was also reported for β_1' [3,67], but it has not been confirmed so far.

In the electron microscopy study of precipitates in a Mg-8 wt.% Zn alloy aged at 200 °C, Gao et al. reported that, contrary to the traditional view of C14 Laves phase MgZn₂, β'_1 rods have a

base centered monoclinic structure (a=25.96 Å, b=14.28 Å, c=5.24 Å, $\gamma=102.5$ deg) that is similar to that of Mg₄Zn₇ with an orientation relationship of $[001]_{\mathrm{Mg_4Zn_7}} \sim \|[0001]_{\alpha}$ and $(630)_{\mathrm{Mg_4Zn_7}} \sim \|(01\overline{1}0)_{\alpha}[20]$. This result is confirmed by a separate TEM study from Singh et al. [68].

In the TEM study of binary Mg- 3 at.% Zn alloys aged at 150 °C, Rosalie et al. reported, rather than single-phase precipitates, β'_1 rods contain a mixture of Mg₄Zn₇ and C14 MgZn₂ phases [55]. The orientation relationship between α -Mg matrix, Mg₄Zn₇ and C14 MgZn₂ follows [0001]_{Mg} || $[010]_{Mg_4Zn_7}$ || $[0001]_{C14}$ and $(11\bar{2}0)_{Mg}$ || $(20\bar{1})_{Mg_4Zn_7}$ || $(0\bar{1}10)_{C14}$ [55]. Some domains of C15 MgZn₂ were also found inside the β'_1 rods [54,55]. The two Laves phase structures have the orientation relationship: $[1\bar{1}00]_{C14}$ || $[110]_{C15}$ and $(0002)_{C14}$ || $(1\bar{1}1)_{C15}$ [54,55].

Based on HAADF-STEM study in Mg-2.2 at.% Zn alloy aged at 200 °C, Bendo et al. also confirmed that [25], in addition to C14 MgZn₂ and monoclinic Mg₄Zn₇, β'_1 precipitates in binary Mg-Zn alloy show a variety of crystal structures, which can be interpreted as 2 dimensional arrangement of the Mg₆Zn₇ elongated hexagonal units and the MgZn₂ rhombic units in Penrose tiling viewed along [2 $\overline{110}$]_{C14} (or [010]_{Mg₄Zn₇}) direction. The two structural units can be tiled to form a series of structures: the crystalline phases (i.e., C14 and C15 MgZn₂ Laves phase), complex 2D quasicrystals (without translational symmetry on the (2 $\overline{110}$)_{C14} plane) and their approximants (i.e., crystalline structures of Mg₄Zn₇ and similar structures). The orientation relationship between α -Mg matrix, domains of C14 MgZn₂ follows [0001]_{Mg} || [2 $\overline{110}$]_{C14} and (11 $\overline{120}$)_{Mg} || (0001)_{C14} [25].

Combining TEM with molecular dynamics simulations, Yang et al. explains that the prismatic dislocations in Mg-Zn system break the symmetry of HCP lattice and further introduce fivefold rings, which facilitate the formation of 2D quasi-crystalline precipitates along the dislocations. Although not explicitly mentioned, the morphology and orientation of the rod-like precipitates are consistent with those of β'_1 [44].

2.2.4 β_2' precipitates

The metastable plate-like precipitates are generally identified as β_2' and form on the basal plane of Mg matrix [3,18,20,21]. Extensive formation of plate-like β_2' coincides with the onset of overaging [18]. The crystal structure of β_2' is confirmed to be C14 MgZn₂ with an orientation relationship of $(0001)_{C14} \parallel (0001)_{Mg}$ and $[11\overline{2}0]_{C14} \parallel [10\overline{1}0]_{Mg}$, as reported in the early

literature [18]. A small fraction of the β_2' precipitates are also reported as laths with the long axis along $[0001]_{Mg}$ and an orientation relationship with Mg matrix same as that of β_1' , i.e., $[11\bar{2}0]_{C14} \parallel [0001]_{Mg}$ and $(0001)_{C14} \parallel (11\bar{2}0)_{Mg}$ [20]. It is suggested that these β_2' laths can be distinguished from the β_1' rods by the larger aspect ratio of the cross section and the near parallelogram shape with the broad surface parallel to $[10\bar{1}0]_{Mg}$ [3]. However, there is no quantitative criterion to differentiate the morphology of a rod from that of a lath. In some papers these laths are also denoted as β_1' [25]. Less commonly, other orientation relationships between β_2' laths and Mg matrix are also reported, e.g., $[11\bar{2}0]_{C14} \parallel [0001]_{Mg}$, $(1\bar{1}06)_{C14} \parallel (\bar{1}010)_{Mg}$ [18,20].

2.3. Open questions

With the advanced characterization techniques, especially HAADF-STEM and 3DAP, the structures of intermetallic compounds and precipitates in alloys can be thoroughly investigated. However, there are on-going debates on the structures and stabilities of phases in Mg-Zn alloys, especially for the metastable precipitates. The key open questions are summarized as the following:

- (1) What are the atomic structures of GP zones in Mg-Zn alloys?
- (2) Why do a hierarchy of structures built by the rhombic MgZn₂ and the hexagonal Mg₆Zn₇ units (e.g., C14 and C15 Laves phase MgZn₂, Mg₄Zn₇, quasicrystals and approximants) coexist in the β'_1 precipitates? What are the relative stabilities of structures within this hierarchy?
- (3) Why do β'_2 precipitates (C14 MgZn₂) predominantly have two distinct orientation relationships with respect to α -Mg?

In the following sections, comprehensive first-principles calculations based on DFT [27,28], CE [29] and MC [30] are performed to fill the knowledge gaps and shed light on the above questions.

3. Methodology

3.1 DFT calculations

First-principles calculations based on DFT [27,28] were employed to optimize the ground-state structures and calculate the energies. The ion-electron interaction was described by the projector augmented plane-wave method [69] and the exchange-correlation functional was described by an improved general gradient approximation of Perdew-Burke-Ernzerhof [70], as implemented in the Vienna ab initio simulation package (VASP, version 5.4) [71,72]. An energy cutoff of 400 eV was

adopted for the plane-wave expansion of the electronic wave functions. The Methfessel-Paxton technique was adopted with smearing parameter of 0.2 eV for integration over k points [73]. The Brillouin zone was sampled by Gamma-centered grids with the k points per reciprocal atom over 8000 [74]. For all the configurations under consideration, all degrees of freedom for the cell, i.e., volume, shape, and internal atomic positions, are allowed to relax for structural optimization. To improve the accuracy of energy calculations, static calculations with the tetrahedron method incorporating Blöchl correction [75] were adopted after structural relaxations.

3.2 Cluster expansion and Monte Carlo simulations

For coherent phase stability, we used first-principles electronic structure methods based on DFT in combination with CE approach to predict the energies of coherent orderings in Mg-Zn system on the lattice of HPC and FCC Mg and select the orderings with low energies. The state of order of Mg and Zn atoms on the parent lattice is described by assigning spin variables, σ_i , to each crystal site i, which takes a value of -1 if a Mg atom resides at the site i and a value of 1 if a Zn atom occupies that site. A particular Mg-Zn arrangement on an N-site lattice is then specified by a vector of occupation variables $\vec{\sigma} = {\sigma_1, \sigma_2, ..., \sigma_N}$. Then, the energy of a given atomic configuration on the fixed parent lattice can be cast into [76,77]:

$$E_f(\vec{\sigma}) = J_0 + \sum_i J_i \ \sigma_i + \sum_{j < i} J_{ij} \ \sigma_i \ \sigma_j + \sum_{k < j < i} J_{ijk} \ \sigma_i \ \sigma_j \ \sigma_k + \cdots$$
 (1)

where J_0 , J_i , J_{ij} , J_{ijk} are the effect cluster interactions (ECIs) for empty, point, pair and triplet clusters. In the CE formalism, ECIs are dependent on the geometry of the corresponding clusters but independent of the atomic occupations [76,77]. Once the ECIs are obtained by fitting Eq. (1) to the energies of known structures, the energy of any configuration can be readily calculated.

The MAPS code in ATAT was used to generate various atomic configurations on the lattice, automate the DFT calculations and construct the CE Hamiltonian [74,78]. Here the training sets of all symmetrically distinct orderings were enumerated up to 18 atoms within the supercell. Then, the ECIs of clusters are obtained by fitting the Hamiltonian to the DFT energies of these orderings using the least square method [74,79]. The leave one out cross-validation score (LOOCV) was used to optimize the selection of the cluster set within a truncated cluster size. In this study, convergence of CE is reached once LOOCV is smaller than 5 meV, no new ground state is predicted, and the ECIs do not change significantly if more configurations from DFT calculations are added. Due to the inherent lattice mismatch between Mg and Zn atoms, many orderings showed

large deviations from the parent lattice sites in DFT calculations due to large lattice distortion. The incorporation of the energy variations from such deviations are beyond the capability of the formulation of CE, which is essentially a generalized Ising-type lattice model for configurational thermodynamics [76,77]. Numerous tests show that deviation from parent lattice would pose challenge to numerical convergence and lead to inaccuracy in predicted energy [78,80]. Therefore, the structures with the lattice distortion larger than 10% were excluded in the current fitting of CE Hamiltonian according to the previously reported numerical tests [81].

The obtained CE Hamiltonian was then subjected to semi-grand canonical Monte Carlo (SGCMC) simulations to calculate thermodynamic properties and phase diagrams at finite temperatures using the EMC2 code in ATAT [30]. The simulation cell is at least 100 Å along each Cartesian direction. The system is considered to reach equilibrium if the energy fluctuations in SGCMC is less than 0.1 meV/atom, which is sufficient for numerical convergence according to previous tests [81]. In SGCMC, the chemical potential is fixed and the structure relaxes to one of the ground states if no constraint on the atomic configuration is applied during the equilibration process [82,83]. Hence, a proper constraint on the atomic arrangements is needed if one wants to sample the metastable or unstable region of the configurational space. To calculate the free energies of GP zones above the HCP convex hull, the possible arrangements of solutes are constrained to the structural units of the corresponding GP zone structures in MC simulations. Phase boundaries on composition versus temperature phase diagrams were then determined by detecting sudden changes (or singularities) in the thermodynamic quantities in SGCMC, as implemented in PHB code of ATAT [30]. In this method, the existing thermodynamic data from MC is fitted using a polynomial, which is then used to predict the next data point. Then MC is performed for the next condition. If the predicted quantity by the polynomial is significantly different from the one calculated by MC, a phase transition is detected. This method roots in the fact that the phase transitions are associated with the sudden changes of thermodynamic quantities (or their derivatives).

3.3 Coherency strain energy calculations

As mentioned, the DFT calculations of many Zn orderings on HCP Mg lattice showed deviation from the ideal lattice sites after full-degree relaxation, which can be caused by the lattice mismatch between Zn and Mg atoms. Therefore, the coherency strain energy (CSE) that shows the

energy penalties of coherency atoms keeping coherency on various crystallographic planes are adopted to analyze the strain energy for Mg and Zn atoms on HCP lattice and its potential effect on the morphology and orientation of coherent precipitates.

For a binary system with composition x, the CSE $\Delta E_{CS}(\vec{k},x)$ on the plane of normal \vec{k} can be calculated as the composition averaged strain energies of the two elements in epitaxial configuration [77]. For non-cubic parent lattice with two independent lattice parameters (e.g., HCP), the strain energies (i.e., $\Delta E_{\rm Mg/Zn}^{epi}(\vec{k},a_1,a_2)$) are obtained from biaxially deformed elements from their own lattice parameters on the epitaxial plane \vec{k} (i.e., $a_1^{\rm Mg}$, $a_2^{\rm Mg}$, $a_1^{\rm Zn}$ and $a_2^{\rm Zn}$) to the common in-plane lattice parameters (i.e., a_1 and a_2) and relaxed in the \vec{k} direction [84–86]:

$$\Delta E_{CS}^{HCP}(\vec{k}, x) = \min_{a_1, a_2} [(1 - x) \Delta E_{Mg}^{epi}(\vec{k}, a_1, a_2) + x \Delta E_{Zn}^{epi}(\vec{k}, a_1, a_2)]$$
 (2)

Noted that, for the basal plane, only one independent in-plane lattice parameter, i.e., a, is needed for optimization, while for the other planes, two independent in-plane lattice parameters are needed. Based on the symmetry of HCP lattice, 3 symmetrically distinct crystallographic planes are chosen to analyze the anisotropy of CSE, including basal plane ($\{0001\}$), and two prismatic planes ($\{10\overline{1}0\}$ and $\{11\overline{2}0\}$).

Here two approaches are adopted to obtain the epitaxial strain energy $\Delta E^{epi}(\vec{k},a_1,a_2)$ in Eq.(2), namely DFT and linear elasticity theory (or harmonic elasticity theory [77,85]). The DFT calculations can capture the anharmonic elastic response of the biaxial deformation [85–87], while the linear elasticity theory only consider the linear elastic response (or harmonic effects) of solid under small lattice distortions within elastic response limit[88,89]. If the lattice mismatch is sufficiently small, $\Delta E^{epi}(\vec{k},a_1,a_2)$ from DFT and the linear elastics would coincide with each other. Therefore, linear elastic result is a reference to reflect the anharmonic effect from DFT result. In linear elasticity theory, $\Delta E^{epi}(\vec{k},a_1,a_2)$ for the constituent Mg or Zn follows [85],

$$\Delta E_{\text{Mg/Zn}}^{epi}(\varepsilon_{2}', \varepsilon_{3}') = \frac{V_{0}}{2} \begin{bmatrix} C_{22}' \varepsilon_{2}'^{2} + C_{12}' \varepsilon_{2}' \left(\frac{C_{12}' \varepsilon_{2}' + C_{13}' \varepsilon_{3}'}{-C_{11}'} \right) + 2C_{32}' \varepsilon_{2}' \varepsilon_{3}' \\ + C_{13}' \varepsilon_{3}' \left(\frac{C_{12}' \varepsilon_{2}' + C_{13}' \varepsilon_{3}'}{-C_{11}'} \right) + C_{33}' \varepsilon_{3}' \end{bmatrix}$$
(3)

where ε'_2 and ε'_3 are the two independently optimized strains on the epitaxial plane, and C'_{ij} is the elastic stiffness tensor in Voigt notation with respect to the in-plane coordinate system, with C'_{11} being the out-of-plane stiffness [85]. The elastic stiffness tensor is calculated from DFT with

normal and shear strain of 1%, and transformed to the in-plane coordinate system [90]. Note that all primed variables are functions of plane normal \vec{k} , which accounts for the anisotropy of elasticity.

4. Results

4.1 Phase structures and stability

To assess the phase stability in Mg-Zn binary system, we calculate the 0 K formation energy for the reported compounds with the atomic structures from Inorganic Crystal Structure Database [91]. The symmetry, lattice parameter, and formation energy of the reported phases collected from previous experiments, the DFT results from Materials Project (MP) [56] and Open Quantum Mechanical Database (OQMD) [92], together with current calculations are shown in Table 1.

The global convex hull constructed on the current calculations are shown as the black line in Fig. 2. The predicted stable phases include Mg₂₁Zn₂₅, C14 MgZn₂ and Mg₂Zn₁₁. Careful examination shows that, Mg₄Zn₇ is 1.2 meV/atom above the convex hull, which is close to the error bar of DFT energy. If such small energy difference is ignored, Mg₂₁Zn₂₅, Mg₄Zn₇ and C14 MgZn₂ lie on the convex hull and are stable structures in Mg-Zn system. This is in agreement from the phase diagrams evaluated experimentally [7,93,94]. According to the criterion by Ravi et al. [95,96], the precipitation process during aging follows the sequential decrease of the energy per solute atom of the precipitates, which can be determined by the slope of the line connecting the precipitate to pure solvent on formation energy (ΔE_f) vs. composition diagram; see Fig. 2. From the current calculations, the slopes for C14 MgZn₂, Mg₄Zn₇ and Mg₂₁Zn₂₅ are determined as -0.2091, -0.2118 and -0.2237 (eV/atom), thus leading to the stability sequence of C14 MgZn₂ \rightarrow $Mg_4Zn_7 \rightarrow Mg_{21}Zn_{25}$. Note that the slopes for C14 $MgZn_2$ and Mg_4Zn_7 are actually very close to each other (with a difference of ~ 3 meV/atom), with Mg₂₁Zn₂₅ slightly more stable than C14 MgZn₂ and Mg₄Zn₇. Therefore, from a thermodynamic point of view, the current calculations explains the coexistence of C14 MgZn₂ and Mg₄Zn₇ in β'_1 rods [25,54,55], which eventually transforms to the equilibrium β phase (i.e. Mg₂₁Zn₂₅).

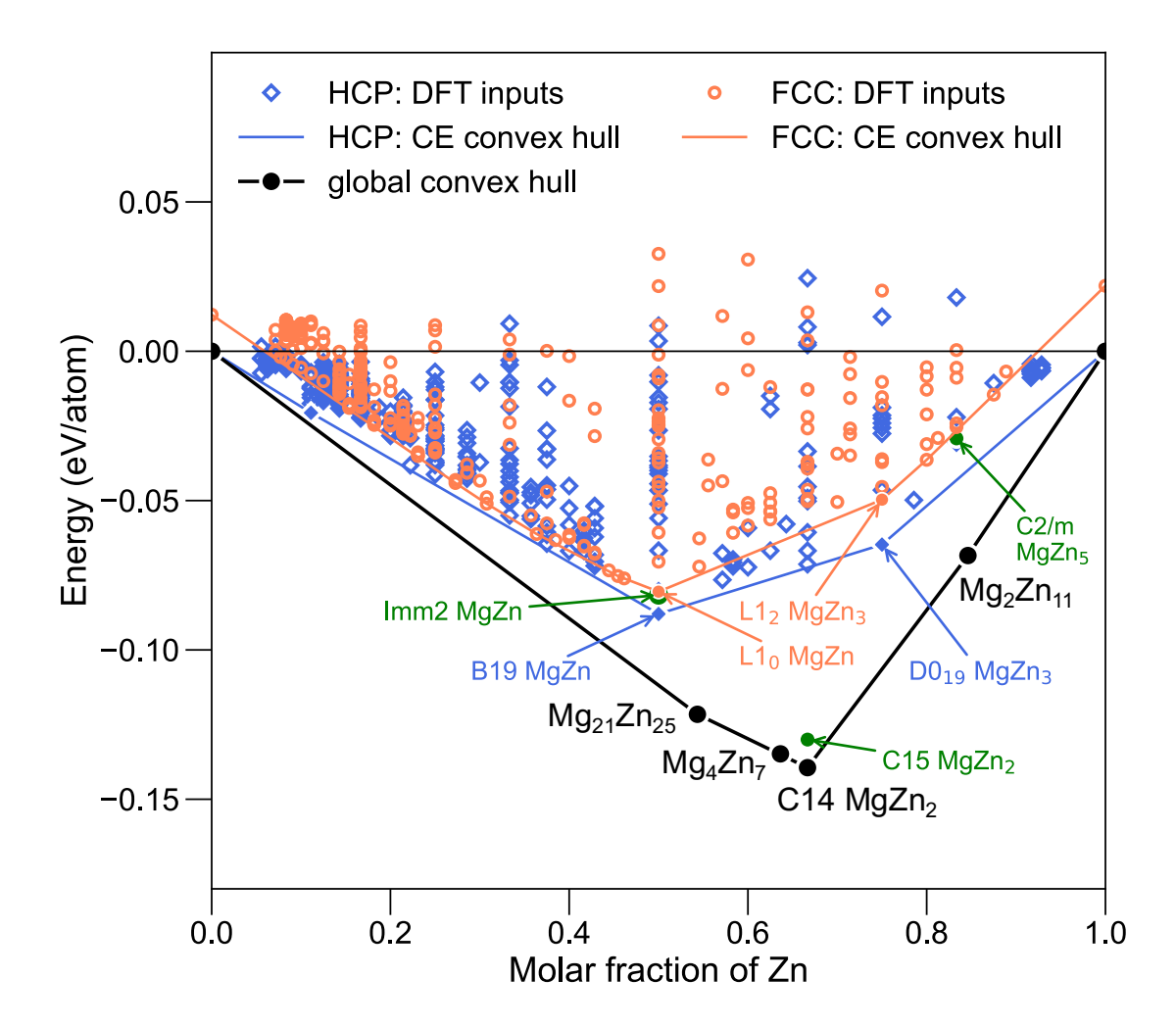


Fig. 2 Formation energies of the experimental observed compounds in Mg-Zn alloy and orderings on FCC and HCP lattice searched by CE. Formation energies are calculated relative to the energy of Mg and Zn on HCP lattice at 0 K. Blue diamonds, orange open circles, green filled circles and black filled circles indicate HCP orderings, FCC orderings, metastable incoherent compounds and stable compounds, respectively.

Table 1. The structural information and formation enthalpies of the compounds and precipitates in Mg-Zn alloys. The first-principles data from Materials Project (MP) [56] and Open Quantum Materials Database (OQMD) [92] are listed together with published experimental and first-principles results.

Phase	Structural information		Lat	ttice parame	Formation enthalpy				
		Method	a/Å	b/Å	<i>c</i> /Å	Reference	Method	Values / kJ/mol-atom	Reference
GP zone	Not reported	Calorimetry				[16]			
	Not reported	Electrical resistivity				[19]			
	Not reported	3DAP				[62]			
	Oblate spheroid on {0001} _{Mg} plane	Laue XRD				[17]			
	Plates on $\{2\overline{1}\overline{1}0\}_{Mg}$ plane	Laue XRD				[17]			
		TEM				[21] [5]			
	Plates on $\{01\overline{1}0\}_{Mg}$ plane	Laue XRD				[61]			
		TEM				[63]			
	Plates on {0001} _{Mg} plane	TEM				[21]			
				T		[5]		1	T = -
$Mg_{51}Zn_{20}$	Orthorhombic, Immm	XRD	14.083	14.486	14.025	[31]	CALPHAD	-4.8, 298K	[97]
(Mg7Zn3)		TEM	14.083	14.486	14.025	[33]	DFT	-5.89, 0K	[98]
(Wig/Zii3)		TEM	14.08	14.49	14.03	[23]	CALPHAD	-5.3, 298K	[93]
	Hexagonal, P63/mmc	XRD	10.66		17.16	[34]	Direct calorimetry	-10.5±3.1, 298K	[99]
		DFT	10.734		17.588	[56]	DFT	-7.14, 0K	[56]
	Orthorhombic, Imm2		5.33	17.16	9.23	[100]	Calorimetry- tin solution	-8.9±0.4, 298K	[101]
		DFT	10.626	17.591	9.177	[92]	DFT	-7.72, 0K	[92]
Mg ₂₁ Zn ₂₅ (MgZn)	Rhombohedral	XRD	25.69	-	18.10	[36]	Calorimetry- acid solution	-12.14±3, 298K	[102]
	C1c1 or C1 2/c1	TEM	16.10	25.79	8.80	[33]	CALPHAD	-9.6, 298K	[97]
							Partial drop- solution	$-7.9 \pm 3.1,$ 298K	[103]
							CALPHAD	-10.4, 298K	[93]
	Trigonal, <i>R</i> 3 <i>c</i>	XRD	25.78	-	8.76	[35]			
		TEM	25.518	-	8.713	[39]	DFT	-12.42, 0K	[98]
		DFT	15.042	15.042	15.042	[56]	DFT	-6.95, 0K	[56]
		DFT	25.4	-	8.6	[92]	DFT	-11.67, 0K	[92]

						Current	DFT	-12.06, 0K	[26]
		DFT	25.78	-	8.76	work	DFT	-11.72, 0K	Current work
			17.24	14.45	5.20	[41]	Calorimetry- acid solution	-13.96±3, 298K	[102]
	Monoclinic, C2/m	XRD	25.96	14.28	5.24	[42]	CALPHAD	-11.0, 298K	[97]
M~ 7"		TEM	25.96	14.28	5.24	[33]	CALPHAD	-10.9, 298K	[93]
Mg_4Zn_7 (Mg_2Zn_3)		TEM	26.69	14.11	5.11	[39]	DFT	-13.22, 0K	[26]
		DFT	26.304	14.141	5.287	[56]	DFT	-13.32, 0K	[56]
	C2/III	DFT	25.8	14.1	5.2	[92]	DFT	-12.93, 0K	[92]
		DFT	26.484	14.185	5.190	Current work	DFT	-13.02, 0K	Current work
	Hexagonal, P63/mmc	XRD	5.15		8.48	[49]	Calorimetry- acid solution	-17.6, 291K	[104]
		XRD	5.221		8.567	[105]	Direct calorimetry	-15.1±1.1, 298K	[99]
		DFT	5.251		8.445	[56]	Partial drop- solution	-7.9 ± 3.1, 298K	[103]
C1.4		DFT	5.188		8.495	[92]	Calorimetry- tin solution	$-10.9 \pm 0.4,$ 298K	[101]
C14 MgZn ₂							Calorimetry- acid solution	$-13.8 \pm 3,298$ K	[102]
							CALPHAD	-11.7, 298K	[97]
							DFT	-13.85, 0K	[98]
							DFT	-12.64, 0K	[56]
							DFT	-13.32, 0K	[92]
							DFT	-13.60, 0K	[26]
		DFT	5.221		8.503	Current work	DFT	-13.41, 0K	Current work
	Cubic, Fd3m	TEM				[54]			
		TEM				[55]			
C15 MgZn ₂		DFT	5.21	5.21	5.21	[26]	DFT	-12.64, 0K	[26]
		DFT	5.234	5.234	5.234	[56]	DFT	-12.93, 0K	[56]
		DFT	5.219	5.219	5.219	Current work	DFT	-12.58, 0K	Current work
Mg ₂ Zn ₁₁	Cubic, Pm3		8.552	8.552	8.552	[59]	Direct calorimetry	-10.0 ± 2.5, 298K	[99]
		TEM	8.415~8.4 62	8.415~8.4 62	8.415~8.4 62	[39]	CALPHAD	-5.8, 298K	[97]

DFT	8.551	8.551	8.551	[56]	DFT	-6.56, 0K	[56]
DFT	8.496	8.496	8.496	[92]	DFT	-6.46, 0K	[92]
DFT	8.519	8.519	8.519	Current	DFT	-6.56, 0K	Current
				work	CALDILAD	0.0.0077	work
					CALPHAD	-9.9, 298K	[93]
					Calorimetry- acid solution	$-8.96 \pm 3,298$ K	[102]
					DFT	-7.11, 0K	[98]
					DFT	-6.66, 0K	[26]

Most early-stage precipitates usually form coherently with the matrix due to the strong constraint from the parent lattice. Therefore, the metastable convex hulls on HCP Mg matrix in Mg-Zn system are calculated with the low energy structures searched by CE. The FCC metastable convex hull is also calculated, considering the formation of FCC phase in some HCP Mg alloys [81]. The symmetrically distinct orderings on both lattices are enumerated for up to 18 atoms to search for the ground states of coherent orderings. The distortion of the structures during structural relaxation are calculated according to the criterion of ATAT [78,81], and these relax away from the parent lattice (i.e., over 10% lattice distortion) are excluded for the CE fitting. All the energies of those orderings within the relaxation range after DFT calculation are shown in Fig. 2 (orange circles for FCC and blue diamonds for HCP). The corresponding convex hulls are built, with the ground state being B19 MgZn and D0₁₉ MgZn₃ for HCP lattice, and L1₀ MgZn and L1₂ MgZn₃ for FCC lattice. The FCC convex hull is higher than that of HCP across all concentration range, which means the orderings on HCP lattice are more stable. However, both convex hulls are well above the global convex hull, making the HCP and FCC ordering phases less stable than ground sates on the global convex hull and thus more difficult to be massively observed in experiments.

4.2 Atomic structures of GP zones

As listed in Table 1, there have been experimentally reported plate-like GP zones on $\{0001\}_{Mg}$ planes [5,21], $\{2\overline{11}0\}_{Mg}$ planes [5,17,21], $\{01\overline{1}0\}_{Mg}$ planes [61,63] and ones without structural information [62] in Mg-Zn alloys. However, these GP zones were rarely clearly characterized in experiments. Therefore, we leveraged DFT combined with CE to predict their potential atomic structures. Here the coherent orderings showing Zn-rich plates (GP sheets) on the reported planes of the Mg matrix are considered to contain the potential GP zones. In addition, those containing low-energy rods (GP rods) and bulk structures are also considered since they are reported to be structurally related to the GP sheets in other Mg alloys [106]. To search the potential GP zones, all the low-energy coherent structures that are within ~ 10 meV/atom above the HCP convex hull with the overall Zn composition less than 50% are examined. The criterion of ~ 10 meV/atom is chosen considering the error bars involved in the methods of DFT and CE. Previously the GP zones within this energy range were reported to be observed in experiments [106]. Using this criterion, two bulk structures are found, i.e., $D0_{19}$ Mg₃Zn and B19 MgZn with the former being 2.7 meV/atom above and the latter on the HCP convex hull, and their detailed atomic structures are shown in Fig. 3(a) and (b), respectively.

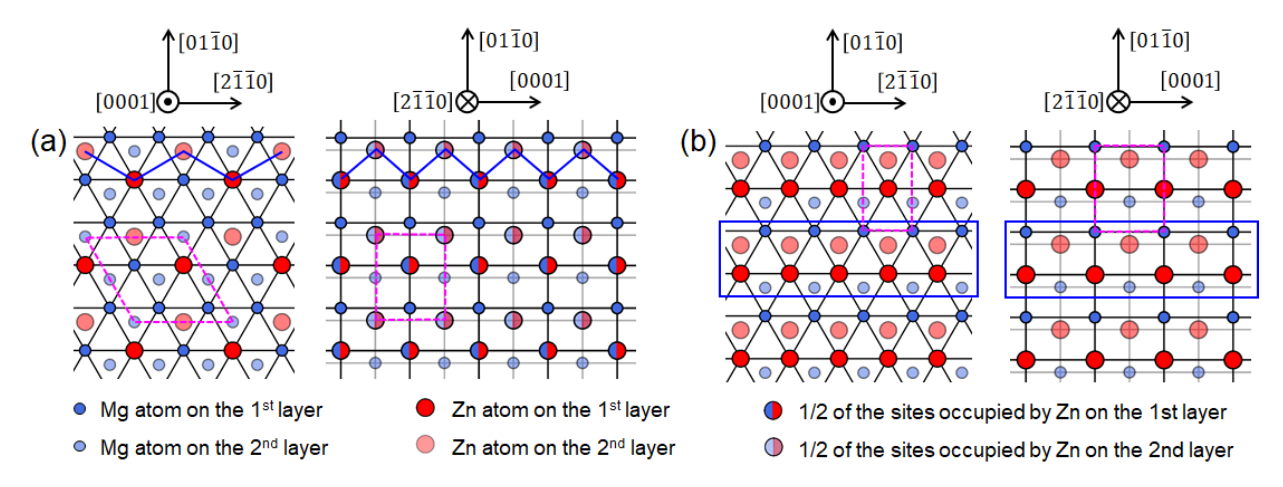


Fig. 3 Schematic crystal structures of (a) $D0_{19}$ Mg₃Zn (2.7 meV/atom above HCP convex hull) and (b) B19 MgZn (on HCP convex hull). The Mg and Zn atoms are represented by blue and red circles, respectively, with the second layers along the [0001] and [$2\overline{1}\overline{1}0$] directions partially transparent to distinguish from the first layer. The dashed purple line indicates the primitive cell. The circles partially in red indicates the fraction of Zn occupancy along the viewing direction. The blue lines indicate the "building block" of the ordering structures.

As shown in Fig.4, the formation energies of structures containing the same type of GP zone are marked with the same symbol (belong to the same family). The difference of structures in a family comes from different relative positions between neighboring GP zones in the Mg matrix. The atomic structures of different GP zones are plot schematically with Mg matrix hidden for convenience. The GP rods are predicted to consist of single and double Zn atomic rows are along the $[2\bar{1}\bar{1}0]_{Mg}$ direction (cyan and brown boxes) with their formation energies marked by cyan 'Y' and brown ' λ ' symbols, respectively. The GP sheets on the $\{0001\}_{Mg}$ plane are predicted to have single or triple Zn-rich layers with the Zn concentration of 50 at.% within the Zn-rich layer (green box in the $[2\bar{1}\bar{1}0]_{Mg}$ direction), and their formation energies are marked by green hexagons. The GP sheet on the $\{2\bar{1}\bar{1}0\}_{Mg}$ plane is predicted to be a monolayer structure with 50 at.% Zn within this layer (blue box in the $[0001]_{Mg}$ direction), and its formation energy is marked by blue square. The GP sheets on the $\{01\bar{1}0\}_{Mg}$ plane are predicted to have zigzagged Zn atoms (purple box) and double-layered Zn atoms (red box) viewed along the $[0001]_{\alpha}$ direction, and their formation energies are marked by purple and red squares, respectively.

The relative stabilities of the predicted structures can be analyzed by the vertical distances of their formation energies to the HCP convex hull. Those with smaller distances are more thermodynamically stable. As shown in Fig. 4, the structure containing the GP sheet on the $\{2\overline{11}0\}_{Mg}$ plane has a distance to the convex hull of 10.2 meV/atom. The most stable structure containing the GP sheet on the $\{0001\}_{Mg}$ plane (the monolayer one) has a distance of 6.6 meV/atom. For GP sheets on the $\{01\overline{1}0\}_{Mg}$ plane, there are two different types, i.e., the zigzagged ones in the D0₁₉ family and the double-layered ones in the B19 family. The most stable structure in the B19 family resides on the HCP convex hull, while the most stable one in the D0₁₉ family has a distance of 7.4 meV/atom. Therefore, within all the GP zones to be potentially observed in experiments, the one containing the double-layered GP sheet on the $\{01\overline{1}0\}_{Mg}$ plane is the most thermodynamically favored, followed by the one with the monolayer GP sheet on the $\{0001\}_{Mg}$ plane, the one with the zigzagged GP sheet on the $\{01\overline{1}0\}_{Mg}$ plane, and finally the one with the GP sheet on the $\{2\overline{1}\overline{1}0\}_{Mg}$ plane. Noted, the structures in Fig. 4 are calculated using small DFT cells, where the constraint from the large Mg matrix on GP zones not fully considered. Further analysis on the effect of this constraint from the Mg matrix on the stabilities of GP zones is detailed in section 4.4.

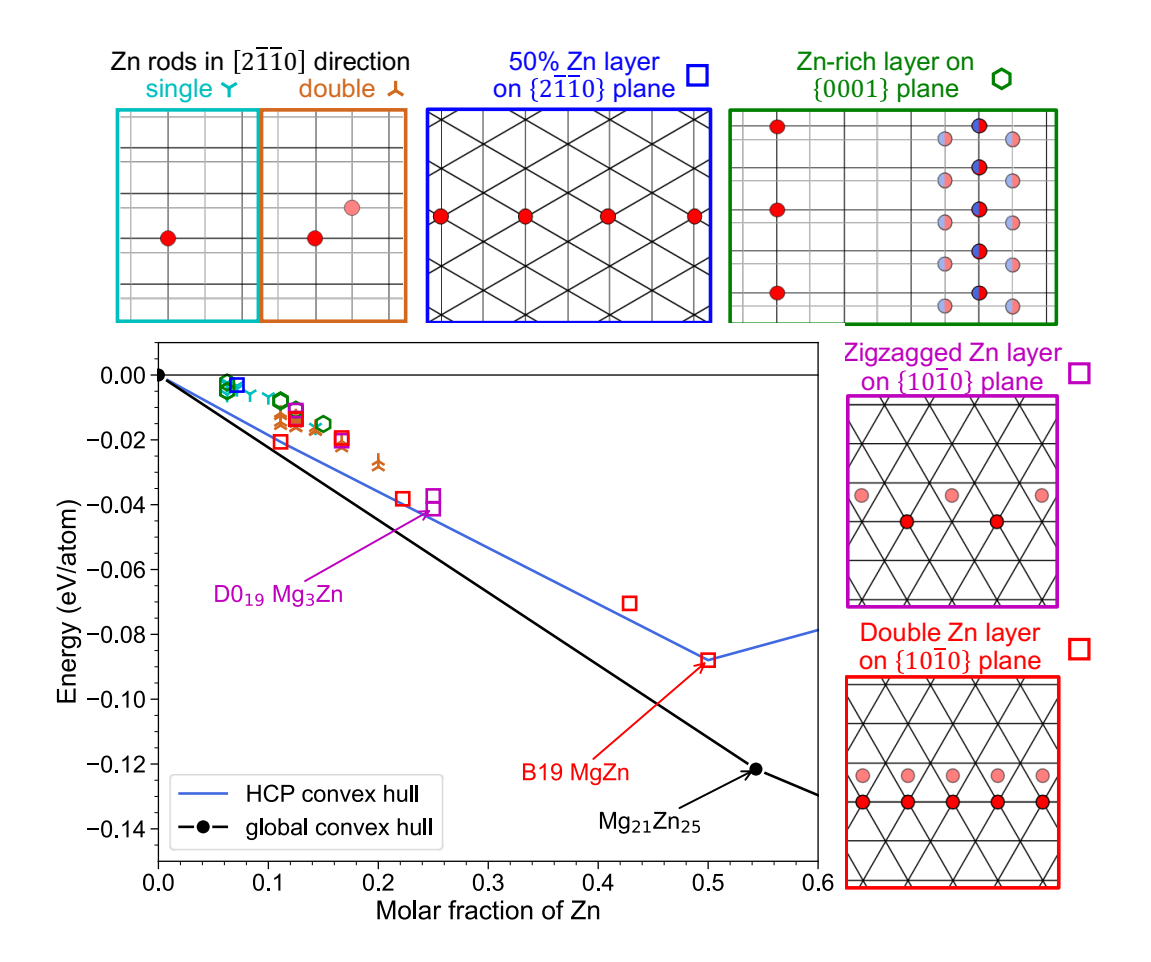


Fig. 4 The ground state formation energies of the predicted GP zones and their schematic crystal structures. In the schematics for structures, the sites that are fully and partially occupied by Zn are indicated using red and red/blue circles, respectively.

Further examination shows that GP zones on the $\{01\bar{1}0\}_{Mg}$ plane are structurally related to the two bulk structures, i.e., D0₁₉ Mg₃Zn and B19 MgZn. The zigzagged GP sheets on the $\{01\bar{1}0\}_{Mg}$ plane are the substructures of the D0₁₉ Mg₃Zn bulk structure, as indicated by blue lines in Fig. 3(a) of the bulk D0₁₉ Mg₃Zn and Fig. 5(a) of a zigzagged Zn GP sheets. Similarly, the double-layered GP sheets on the $\{01\bar{1}0\}_{Mg}$ plane are substructures of the B19 MgZn bulk structure, as indicated by the blue box in Fig. 3(b) of the bulk B19 MgZn and Fig. 5(b) of a double layered Zn GP sheets. Overall, the GP sheets on the $\{01\bar{1}0\}_{Mg}$ plane can be regarded as the mixtures of pure Mg and the building blocks of the predicted bulk structures, and the ratio of the two mixing "components" can change with the overall Zn concentration in the Mg matrix.

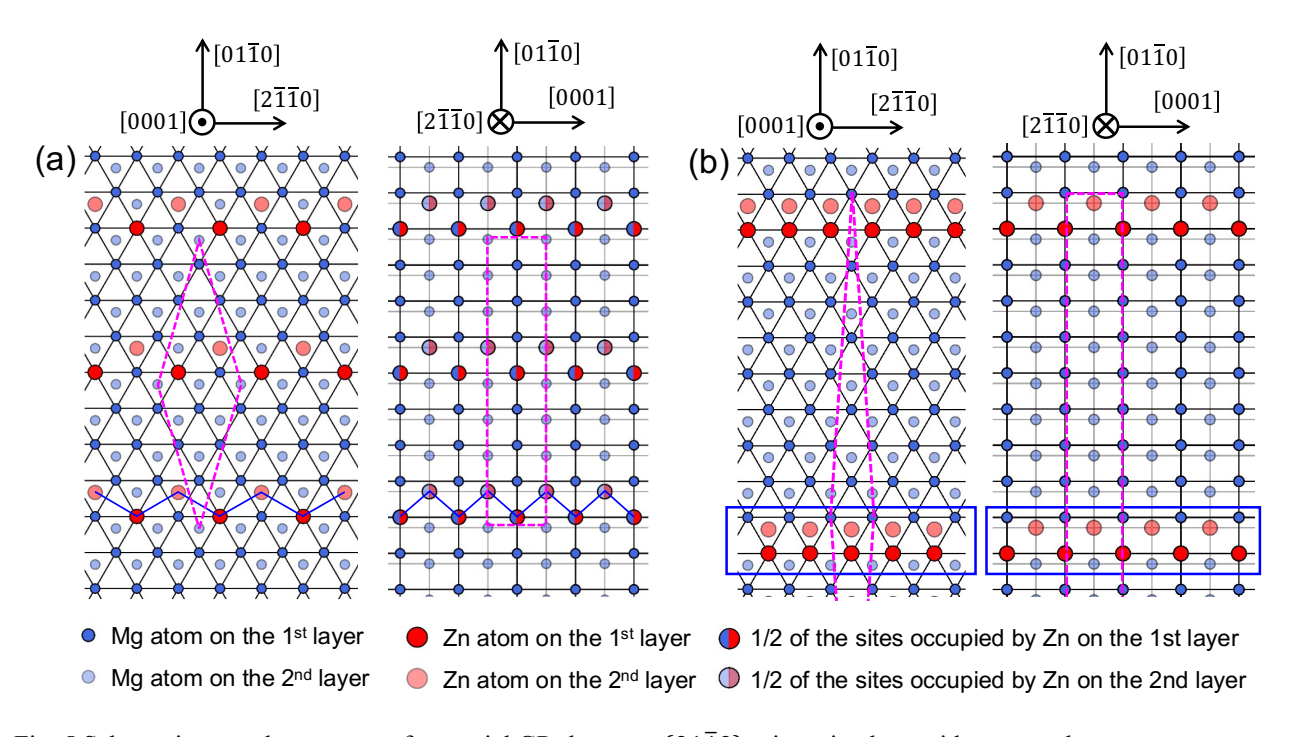


Fig. 5 Schematic crystal structures of potential GP sheets on $\{01\overline{1}0\}$ prismatic plane with energy close to convex hull (5meV/atom): (a) GP sheet resembling D0₁₉ Mg3Zn; (b) GP sheet resembling B19 MgZn.

4.3 Finite temperature stability of GP zones

At finite temperatures, the disordering of site occupation will lead to configurational entropy that affects the stability of GP zones. Here the equilibrium between Mg solid solution and potential GP sheets are examined by the SGCMC simulation and compared with experiments. To demonstrate how the phase boundaries are calculated, the free energies of Mg solid solution and potential GP sheets on $\{01\overline{1}0\}_{Mg}$ plane with zigzagged Zn (Fig. 5(a)), as well as the common tangent for phase equilibrium are shown in Fig. 6(a). The SGCMC simulation without further constraints yields the free energies for single phase regions, but not the metastable or unstable regions [81]. Therefore, in the current MC of GP zones, the atomic arrangements are constrained to the structural template to sample the configurational states related to the corresponding GP zones above the HCP convex hull, which are in metastable states. For example, the free energy curve of the zigzagged GP zone in D0₁₉ family is calculated using Monte Carlo by only allowing the Zn atoms in the GP zone to be switched to Mg, while the switching from Mg to Zn is prohibited. In this way, the Zn atoms in the intermediate structures are either isolated in Mg matrix or form part of the zigzagged GP zone and Mg-rich solid solutions.

Using this method, the phase boundaries (i.e., GP zone solvus) between Mg solid solutions and predicted structures containing GP sheets on $\{01\overline{1}0\}_{Mg}$, $\{2\overline{1}\overline{1}0\}_{Mg}$ and $\{0001\}_{Mg}$ planes are calculated and compared with the alloy composition vs. temperatures of experimentally reported GP zones. The GP zone solvus is the boundary between single phase region of the Mg-rich solid solution and dual-phase region of the Mg-rich solid solution and the GP zone, with the upper-left side of the curve being Mg-rich solid solution and the lower-right side being the mixture of Mg-rich solid solution and GP zone. Noted, the listed experimental data points are the alloy composition vs. the temperature at which the GP zones were observed, not the experimentally measured phase boundary. Therefore, as long as the experimental data points for a specific GP zone fall below the solvus, the calculation agrees with the experiments.

As shown in Fig. 6(b), the calculated solvi for GP zones on $\{01\overline{1}0\}_{Mg}$ and $\{0001\}_{Mg}$ planes are above the corresponding experimental conditions, while the solvus for GP zones on $\{2\overline{1}\overline{1}0\}_{Mg}$ plane is below some of the experimental conditions. For GP zones on $\{01\overline{1}0\}_{Mg}$ plane, the phase boundary calculations show that GP sheets with double-layered Zn (the B19 family) is more stable

than the zigzagged GP sheets. However, the double-layered GP sheet is predicted to transit to disordered solid solutions at very high temperatures (e.g., \sim 750 K for Mg-1 at.% Zn alloy), which are unrealistically stable as compared with experiments [17,63]. This indicate that the stability of the double-layered GP sheet is overestimated. The origin to this discrepancy is attributed to the lack of the constraint from Mg matrix to the GP sheets in the small structures in the training set of CE; see Section 4.4 for detailed discussion. In comparison, the calculated solvi for zigzagged GP zone on $\{01\overline{1}0\}_{Mg}$ plane (blue line in Fig. 6(b)) and single layer GP zone on $\{0001\}_{Mg}$ plane (green line in Fig. 6(b)) are slightly above the corresponding experimental conditions, which indicates agreement between calculations and experiments. For the GP zone on $\{2\overline{1}10\}_{Mg}$ plane, the calculated solvus (brown line in Fig. 6(b)) breaks down due to the appearance of other ordering structures in MC simulations. Comparison with the corresponding experimental data indicates that the stability of GP zone on $\{2\overline{1}10\}_{Mg}$ plane is underestimated.

The discrepancies between the calculated solvi and experiments can be attributed to the approximations and uncertainties involved in calculations and experiments. In the DFT and CE calculations, the typical error bars of energy are approximately 1 and 5 meV/atom, respectively, which is insufficient to exactly reproduce experimental phase boundary. Additionally, the neglected effects (e.g., free energy due to lattice vibrations) in DFT can also contribute to the error in the estimation of the GP zone solvus. Experimentally, the detailed atomic structures of GP zones are not reported and the difference between the predicted atomic structures and the ones in experiments will contribute to the discrepancy. Lastly, some experimental characterization of GP zones in Mg-Zn alloys are considered insufficient [3,21], indicating uncertainties in previous experiments. Nonetheless, with configurational thermodynamics from only short-ranged interactions in CE, the calculations for zigzagged GP zone on $\{01\overline{1}0\}_{Mg}$ plane and single layer GP zone on $\{0001\}_{Mg}$ plane shows reasonable agreement with experiments, indicating the importance of solute ordering during the formation of GP zones.

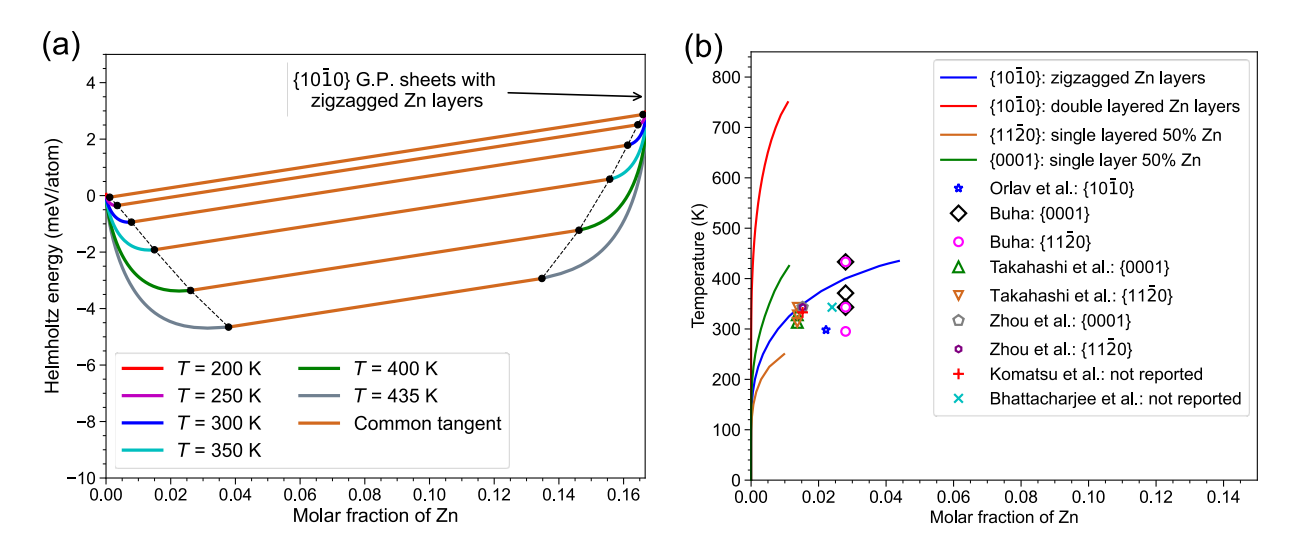


Fig. 6 The stability of the predicted GP zones at finite temperatures from Monte Carlo calculations and experiments: (a) Free energies and common tangents for the equilibrium between Mg solid solution and GP sheets on {0110} plane; (b) The calculated phase boundaries (solid lines) between Mg solid solution and GP zones, compared with the aging temperatures and alloy compositions where various GP zones were observed (symbols).

4.4 Effects of the coherency strain on the stabilities of GP zones

Comparison between experiments and the analysis at finite temperatures indicate that the stability of the double-layered GP sheet on the $\{01\overline{1}0\}_{Mg}$ plane is overestimated, i.e., unrealistically high transition temperature of its solvus. However, this stability analysis is based on energies from CE, where relatively small DFT cells (≤ 20 atoms) are used in the training set. As such, the number of atoms in the Mg matrix is limited; see the DFT cells marked by dashed purple lines in Fig. 5. This means the constraint from the Mg matrix on the GP zones can be incorrectly estimated compared with that in experiments. In our previous tests, the constraint from Mg matrix can slightly alter the relative stabilities between different GP zones calculated in small DFT cells [107]. Since this constraint comes from the coherency strain between GP zones and the matrix due to the lattice mismatch, Zn-concentration dependent CSE are adopted to analyze the effect of coherency strain on stabilities of GP zones. Here CSE were calculated on $\{0001\}_{Mg}$, $\{2\overline{110}\}_{Mg}$, and $\{01\overline{10}\}_{Mg}$ planes, on which plate-like GP zones were experimentally reported to reside.

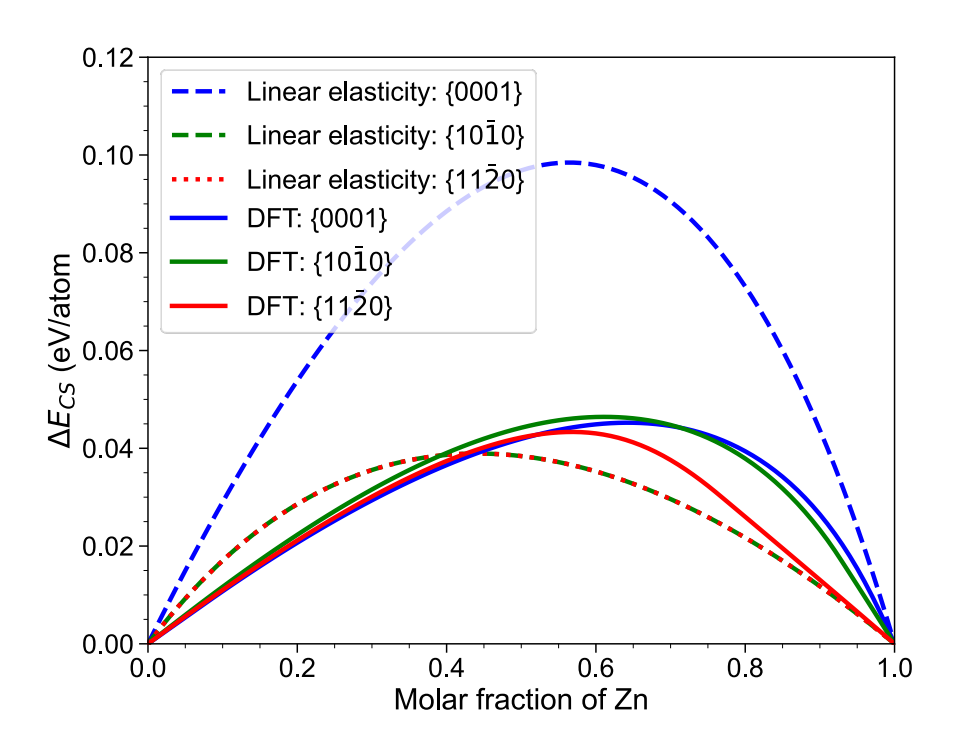


Fig. 7 The coherency strain energy of HCP Mg-Zn alloys as a function of Zn concentration on basal and prismatic planes calculated by DFT and linear elasticity theory

The CSE calculated from linear elasticity theory based on Eq. (3) are shown as dashed lines in Fig. 7. The CSE on the basal plane is significantly larger than those on the prismatic planes. This can be expected from the much larger mismatch along the a than the c axis between HCP Mg and HCP Zn, i.e., $\delta_a = 16.6\%$ and $\delta_c = 4.5\%$ based on the lattice mismatch defined by $\delta_a = (a_{\rm Zn} - a_{\rm Mg})/a_{\rm Mg}$ [108]. However, the linear elasticity approach cannot consider the anharmonic lattice response, which is expected for Mg-Zn system, especially for the large lattice mismatch on the basal plane. Conversely, the anharmonic effects are incorporated in CSE calculated from DFT as shown by the solid lines in Fig. 7, which reveals a similar CSE on the basal and the two prismatic planes. Therefore, the large lattice mismatch on the basal plane is beyond the validity of linear elasticity and the CSE on this plane is overestimated consequently. Similar overestimation of the strain energy from linear elasticity was also reported for Cu [109]. At the Mg-rich side, the close CSE from DFT on the three planes means absence of a single epitaxially soft plane, and the three planes are almost equally favored in terms of coherency strain. This agrees with the fact that GP sheets on these planes are experimentally reported (Table 1), as opposed to the case of Al-Cu alloys, where GP zones are only observed on (001) plane [110].

As shown in Fig. 7, the CSE is proportional to the Zn concentration at the Mg-rich side. This means the CSE penalties increase for GP zones of higher Zn concentrations in a large Mg matrix. To focus on the role of the Zn concentration, the analysis is performed for the two types of GP zones both residing on the $\{01\overline{1}0\}_{Mg}$ plane, i.e., the double-layered one in the B19 family and the zigzagged one in the D0₁₉ family, so that the effect on CSE due to crystallographic orientations is excluded. The double-layered GP sheet in the B19 family has 100 at. % Zn within the sheet, while the zigzagged one in the D0₁₉ family has 50 at. % Zn within the sheet. Thus, the CSE penalty on the double-layered GP sheet is larger than that on the zigzagged GP sheet when they are in large Mg matrixes of the same size. Consequently, the double-layered GP sheets will be destabilized by CSE compared with the zigzagged one.

To confirm the trend of increased CSE with larger Zn concentration, a double-layered GP sheet in the B19 family and a zigzagged GP sheet in the D0₁₉ family are embedded in DFT supercells with the same large Mg matrixes. The Mg matrix consists of 42 layers of Mg along $[10\overline{1}0]_{Mg}$, which was tested to be sufficiently large to eliminate the interaction between GP sheets due to the periodic boundary conditions, as shown in Fig. 8. After DFT relaxation, the solutes in GP sheets do not move due to the symmetry of DFT cells, while the Mg atoms move towards the GP sheets due to the coherency strain. In comparison, the Mg atoms around the double-layered GP sheet in B19 family show much larger displacements than those around the zigzagged GP sheet in D0₁₉ family, which indicates a larger CSE penalty for the double-layered GP sheet.

The destabilization of the double-layered GP sheet in B19 family is confirmed by directly comparing the formation energies of the two supercells, where the constraint from the large Mg matrix on GP zones is better realized than the previous small cells in Fig. 5. The distance of the formation energy of the zigzagged GP sheet to the HCP convex hull is 2.2 meV/atom, while that of the double-layered GP sheet is 4.5 meV/atom. Therefore, with the constraint from Mg matrix, the zigzagged GP zone will be slightly favored than double-layered GP zone. Considering that this energy difference is close to the error bar of the DFT energy, both GP zones are likely to be observed in experiments. This is consistent with the observation of GP sheets on $\{01\bar{1}0\}_{Mg}$ plane in Mg-5.78Zn-0.44Zr wt.% alloy[63], as shown in Fig. 9. Careful examination of the HAADF-STEM image shows that the zigzagged GP zones (yellow arrows in Fig. 9) can be observed. Besides the zigzagged GP zones, there are also GP zones with the same thickness of zigzagged

ones, but denser Zn and clearly a different pattern from the zigzag, as marked by the orange arrow in Fig. 9. This GP zone probably belongs to the B19 family.

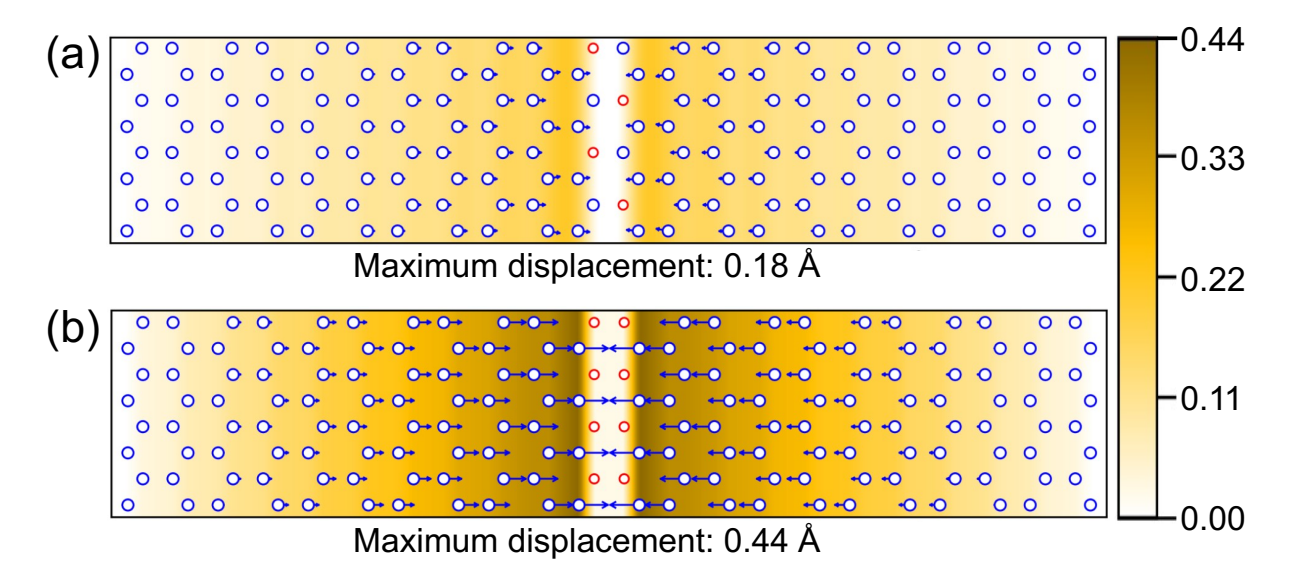


Fig. 8 The large supercell containing (a) a GP sheet that resembles D0₁₉ Mg₃Zn phase, (b) a GP sheet that resembles B19 MgZn phase. The displacements of Mg atoms after relaxation in DFT are marked with arrows, which indicates a larger CSE with GP zones resembling B19 MgZn.

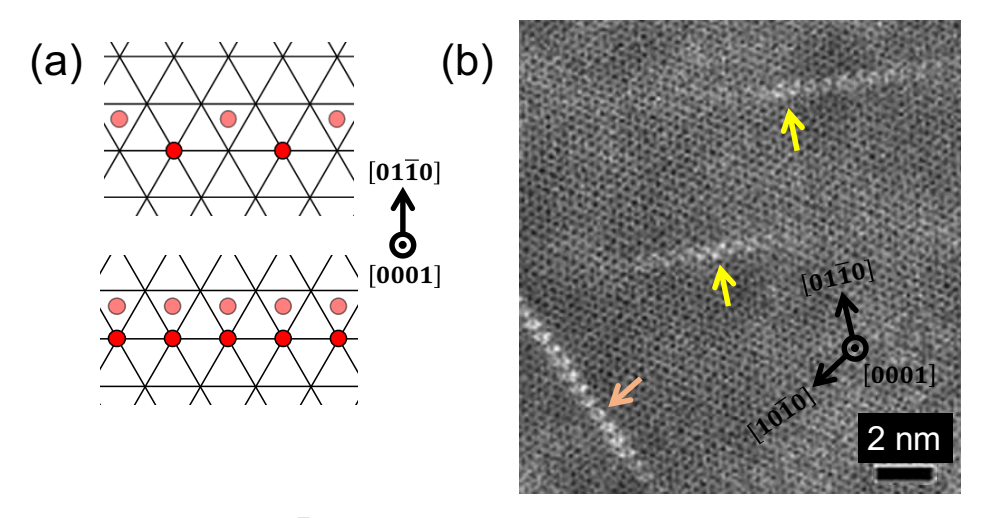


Fig. 9 (a) The predicted GP sheet on $(01\bar{1}0)_{\alpha}$ plane, and (b) experimentally observed nanoscale prismatic GP sheets on $\{01\bar{1}0\}$ plane of Mg matrix in Mg-5.78Zn-0.44Zr wt.% (Mg-2.23Zn-0.12Zr at. %) alloys [63], where Zr works as the grain refiner [64,65]. Note that zigzagged pattern of Zn can be vaguely observed. Fig. (b) is adapted from [63].

4.5 Structure and stability of β'_1 precipitates

 β_1' precipitates have rod-like morphology along [0001]_{Mg} direction and are formed in the peak-aged binary Mg-Zn alloys [18,20,62]. Recent TEM and HADEF-STEM observations [25,44,55] show that the crystal structure of β_1' is complex. Specifically, on the cross sections of the rods as shown in Fig. 10(a), various arrangements of the MgZn₂ rhombic units and the Mg₆Zn₇ elongated hexagonal units on $(2\overline{110})_{C14}$ plane lead to precipitates that are totally or partially composited by C14 MgZn₂, C15 MgZn₂, Mg₄Zn₇, 2D quasicrystals and approximants. To study the stability of β_1' , the stabilities of this hierarchy of structures built by the MgZn₂ rhombic units and the Mg₆Zn₇ elongated hexagonal units are needed to be analyzed.

To probe the huge structural and compositional space of these complex crystalline structures, we built two structures, i.e., $Mg_{32}Zn_{59}$ and Mg_8Zn_{11} , using the two basic units and analyze them together with other decagonal quasicrystal approximants, i.e., Mg_4Zn_7 , $Mg_{29}Zn_{48}$, $Mg_{22}Zn_{34}$, $Mg_{28}Zn_{41}$ from the Alloy Database by Mihalkovic et al. [98]. The structural files of these phases can be found in Supplementary Materials. Here only three phases, i.e., Mg_4Zn_7 , Mg_8Zn_{11} and $Mg_{22}Zn_{34}$ are selected as examples to illustrate the detailed atomic structures, as shown in Fig. 10(b)-(d), respectively. Viewed along $[010]_{Mg_4Zn_7}$ (or $[2\overline{110}]_{C14}$) direction, their primitive cells are indicated in dashed purple line, the two basic units in dashed black lines and structural features of C14 and C15 from the rhombic units in blue and green solid lines, respectively. Mg_4Zn_7 in Fig. 10(b) has the elongated Mg_6Zn_7 hexagonal units at the four corners of the quadrilateral primitive cell, the $MgZn_2$ rhombic units forming C14 at a pair of opposite sides of the quadrilateral and C15 within the quadrilateral. Similarly, Mg_8Zn_{11} in Fig. 10(c) have the Mg_6Zn_7 elongated hexagonal units at the four corners of the quadrilateral primitive cell, but no $MgZn_2$ rhombic units within the cell compared with Mg_4Zn_7 . $Mg_{22}Zn_{34}$ in Fig. 10(d) have the two units arranged in a rotational way, leading to the structural feature of the five-pointed star.

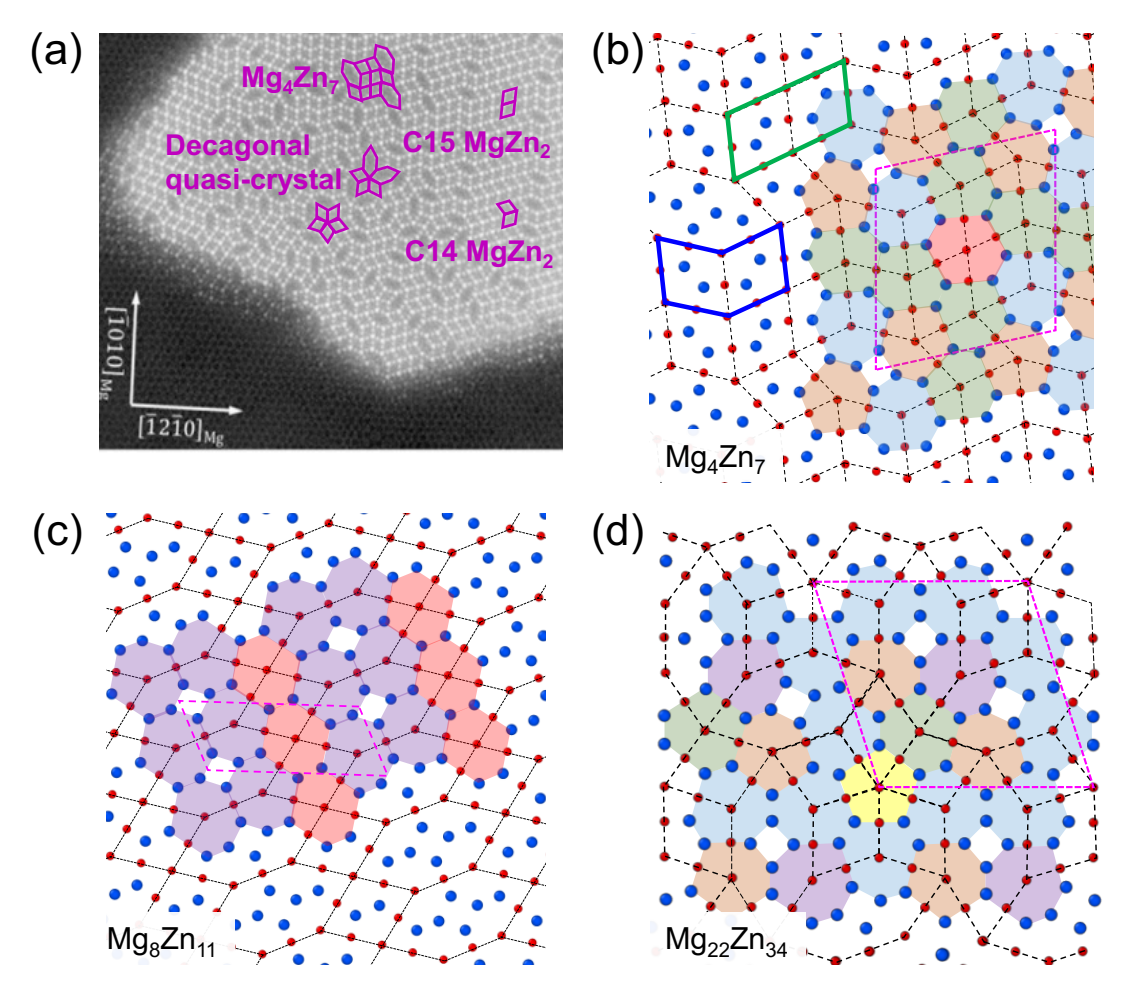


Fig. 10 (a) The cross section of a β_1' rod on $(0001)_{Mg}$ plane adapted from [25], (b) atomic structure of Mg₄Zn₇, (c) Mg₈Zn₁₁, (d) Mg₂₂Zn₃₄ viewed along direction equivalent to $[2\overline{1}\overline{1}0]_{C14}$. The blue and red spheres represent Mg and Zn atoms respectively. The basic units are indicated by thin dashed black lines. The primitive cells are indicated by dashed pink lines. The blue and green lines indicate the structural features of C14 and C15 MgZn₂ phase, respectively. The colored polygons indicate different icosahedra.

The formation energies of the six structures from DFT are shown with global convex hull in Fig. 11, where Mg₃₂Zn₅₉ (-137.9 meV/atom), Mg₄Zn₇ (-134.8 meV/atom), Mg₂₉Zn₄₈ (-133.4 meV/atom) and Mg₂₂Zn₃₄ (-130.0 meV/atom) are within 1 meV/atom from the global convex hull, which essentially reside on the convex hull considering that the error bar of DFT energies. In contrast, Mg₂₈Zn₄₁ (-126.4 meV/atom) and Mg₈Zn₁₁ (-106.9 meV/atom) are 2.5 and 19.8 meV/atom above the global convex hull, respectively. With the increasing Zn concentration, these structures are more stable with structurally decreasing portion of the Mg₆Zn₇ elongated hexagonal units and increasing portion of the MgZn₂ rhombic units based on their relative positions to the global convex hull. Therefore, it is inferred that the MgZn₂ rhombic unit is more

thermodynamically favored than the Mg₆Zn₇ elongated hexagonal unit within β'_1 rods, while the latter are formed due to the Mg enrichment in the local regions. Thus, a general trend is expected for the stabilities of crystalline structures built by the MgZn₂ rhombic and the Mg₆Zn₇ hexagonal units: as the fraction of rhombic units (or Zn concentration) increases, the structures in this family become more stable. This means that there are many structures with large portions of the MgZn₂ rhombic units, especially when forming C14 MgZn₂, residing on the global convex hull, which is consistent with many observed β'_1 rods having large domains of C14 MgZn₂ in experiments [25,55,111].

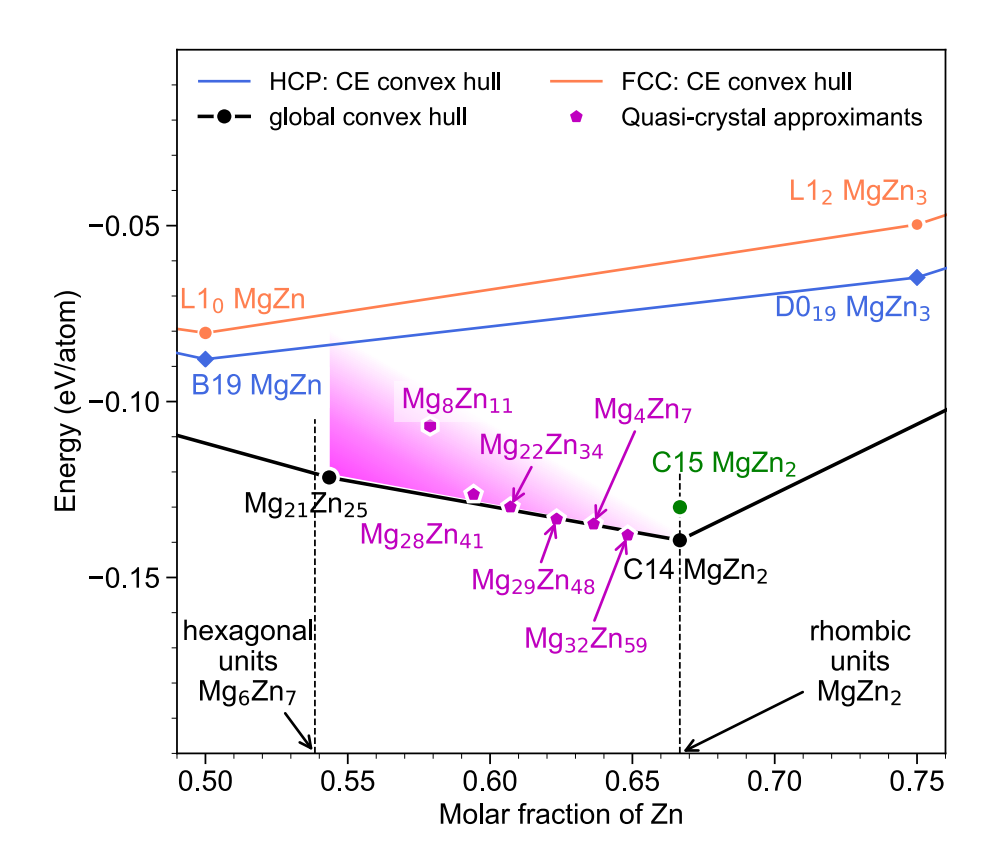


Fig. 11 Formation energies and relative positions to the convex hulls of six structures formed by the MgZn₂ rhombic and Mg₆Zn₇ elongated hexagonal units.

With various arrangements of the two basic units, the crystalline structures can have large primitive cells (e.g., hundreds of atoms or more), and the upper limit is the structures with infinitely large cells, i.e., 2D quasicrystal with the lack of translational symmetry on the plane equivalent to $\{2\overline{110}\}_{C14}$ within β_1' precipitates [25,44]. Several independent experiments revealed the existence

of 2D decagonal quasi-crystalline structures [25,44]. These decagonal quasi-crystalline structures can be built from relatively simple icosahedra with 13 atoms [44]. Since these 2D quasicrystals and their approximants share similar local structures, Mg₄Zn₇, Mg₈Zn₁₁ and Mg₂₂Zn₃₄ in Fig. 10(b)-(d), respectively, are used for illustration. These approximants are built from 6 types of icosahedral chains packed by simple icosahedra along the direction equivalent to [0001]_{C14} or [001]_{Mg4Zn7}, identified by different colors. The arrangement of green and red icosahedral chains leads to the zigzagged and aligned arrangements of the MgZn₂ rhombic units corresponding to C14 and C15 MgZn₂, respectively. The yellow one corresponds to the five-pointed star. Icosahedral chains in other colors are on the corners of the Mg₆Zn₇ elongated hexagonal units. Thus, from the DFT calculations, it is inferred that the energies of these clusters are higher than the green ones leading to C14 MgZn₂. Rather than only determined by thermodynamic stability, the specific atomic structure of the quasicrystal is very sensitive to local atomic environment (e.g., composition and structural defect) and is determined by the competition between the assimilation of the icosahedral clusters with relative lower energies and the trapping of local configurations due to suppressed kinetics [112,113].

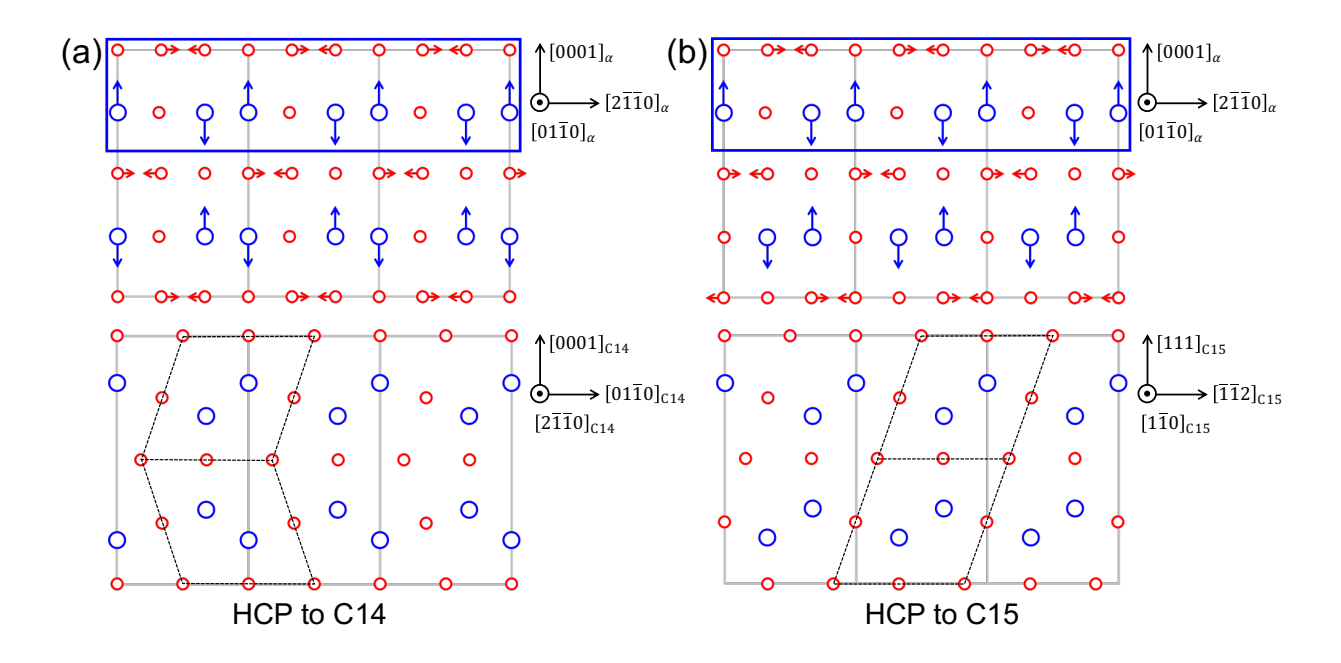
Based on their HAADT-STEM results, Bendo et al. reported that there is a positive correlation between the aspect ratios of the $(0001)_{\alpha}$ cross-section of β'_1 precipitates and the Zn/Mg ratios within β'_1 . [25] Combining this trend with the one in current stability analysis, there is a further correlation between the stability and morphology of β'_1 . Those β'_1 with lower Zn concentration (more hexagonal Mg₆Zn₇ units) and correspondingly a smaller cross-sectional aspect ratio following the rod-like morphology is less stable. Oppositely, those β'_1 with higher Zn concentration (more rhombic MgZn₂ units) and correspondingly a lager cross-sectional aspect ratio following the lath-like morphology is more stable.

5. Discussion

It has been reported that both C14 (zigzagged-packed MgZn₂ rhombic units on (2110)_{C14} plane) and C15 MgZn₂ (aligned-packed MgZn₂ rhombic units on [010]_{C15} plane) Laves phases can be formed directly from the relaxation of HCP orderings [26,114]. Detailed analysis in the current study shows that both phases can be formed from the orderings with same ordered unit layers but stacked differently along [0001] direction of the HCP lattice. As shown in the blue rectangle in Fig. 12, such unit layer is characterized by one layer of Zn on the basal plane and another layer of each Zn atom 6-fold coordinated by Mg atoms on the neighboring basal plane. If

the ordering units are stacked along the $[0001]_{\alpha}$ direction without shift on basal plane, relaxation of such structures leads to the C14 MgZn₂ phase (Fig. 12(a)). Alternatively, if adjacent ordering units are shifted by a along $[2\overline{1}\overline{1}0]_{\alpha}$ direction, relaxation would lead to C15 MgZn₂ phase (Fig. 12(b)).

For both cases, during relaxation, atoms on the pure Zn layers move within this layer to form the Kagome network, and Mg atoms on the adjacent layers move upward or downward along $[0001]_{\alpha}$ direction towards the open area of the Kagome nets on the neighboring layers [26,114]. The atomic displacements during the structural relaxation are indicated by the arrows in Fig. 12. The changes of formation energies along the linearly interpolated transformation pathways are shown in Fig. 12(c), where no energy barrier is observed, indicating both transitions proceed instantaneously. Specifically, the energies of the HCP orderings before transformation are the same while C14 (-139.5 meV/atom) is more stable than C15 (-130.4 meV/atom) at the end of the transformation path, which explains the prevalence of C14 over C15 in Mg-Zn alloy system. These transformation paths lead to orientation relationship with the Mg matrix of $(0001)_{C14} \parallel (0001)_{Mg}$ and $[1\bar{1}00]_{C14} \parallel [11\bar{2}0]_{Mg}$ for C14 MgZn₂ and $(111)_{C15} \parallel (0001)_{C14}$ and $[1\bar{1}0]_{C15} \parallel [2\bar{1}\bar{1}0]_{C14}$ for C15 MgZn₂. Note that these orientation relationships for C14 and C15 MgZn₂ with HCP Mg agree with the experimentally observed orientation relationships between β'_2 laths and β'_1 rods with the Mg matrix [18,25].



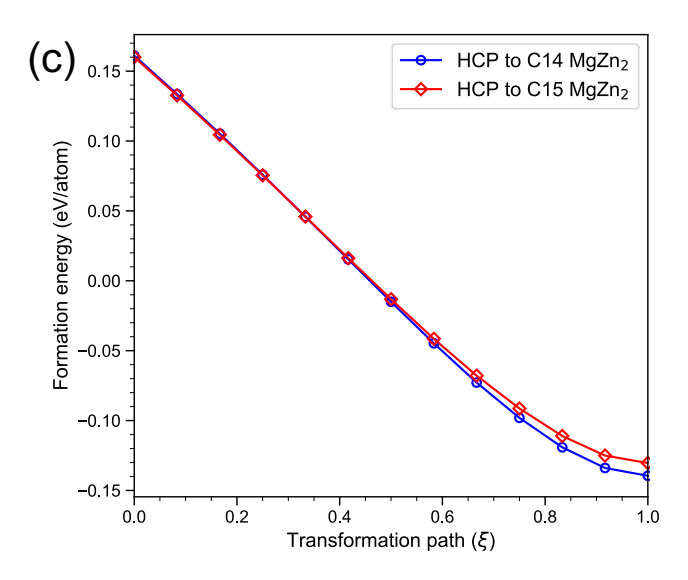


Fig. 12 Transformation paths from HCP ordering phases to C14 and C15 MgZn₂: (a) atomic displacements of HCP ordering (upper) that leads to C14 MgZn₂ (lower); (b) atomic displacements of HCP ordering (upper) that leads to C15 MgZn₂ (lower); (c) Changes of formation energies along the linearly interpolated transformation paths. Note that the blue and red circles denote Mg and Zn, respectively.

Based on the OR between α -Mg and C14 MgZn₂ determined by the above transformation paths, the origin of the two major distinct orientation relationships of C14 MgZn₂ in β'_2 with α -Mg are discussed, i.e., β'_2 plates on the $(0001)_{\alpha}$ plane with $(0001)_{C14} \parallel (0001)_{Mg}$ and $[11\bar{2}0]_{C14} \parallel [10\bar{1}0]_{Mg}$ (denoted as OR1) and β'_2 laths with $[0001]_{C14} \parallel [11\bar{2}0]_{\alpha}$ and $(11\bar{2}0)_{C14} \parallel (0001)_{\alpha}$ (denoted as OR2). [18,20] The β'_2 plate with OR1 is consistent with the OR determined by the discussed transformation path. On the other hand, the β'_2 lath with OR2 (observed along with β'_1) have the similar structure, orientation relationship and morphology as some β'_1 precipitates with a large cross-sectional aspect ratio [20,25]. Therefore, β'_2 lath with OR2 is a structural limit of β'_1 precipitates built almost entirely by C14 MgZn₂.

Based on the combined information of the ORs, the stability analysis of structures in Sec. 4, and the observation of precipitation in experiments, it is inferred that β'_2 precipitates with the two distinct ORs and morphologies forms in different paths. The plate-like β'_2 precipitates with OR1 can be formed from (i) the relaxation of the coherent ordering on HCP Mg matrix as discussed, and further coarsens to plates on basal plane of α -Mg; (ii) the decomposition of the less stable β'_1 rods to the stable C14 MgZn₂, which corresponds to the decreased amount of β'_1 rods and increased amount of β'_2 plates with OR1 in prolonged aging process [18]. In contrast, the lath-like β'_2

precipitates with OR2 are formed in the same way as β'_1 rods but with very large fraction (or completely) of the structure being C14 MgZn₂. Additionally, it is suggested that β phase has a structure of Mg₂₁Zn₂₅ (space group R $\bar{3}$ c), which consists of hexagonal prisms of C14 MgZn₂ and Mg-rich transition regions [38]. Note that β'_2 (i.e., the C14 Laves phase) is a very stable compound and is very unlikely to transform to other structures at the common aging temperatures of Mg alloys, e.g., 300 K (27 °C) to 500 K (227 °C), where the kinetics is suppressed. Therefore, in practical aging treatment, the formation of β precipitate is likely to be suppressed due to low temperatures and difficult to be observed, although β is the equilibrium phase with α -Mg [20,39,62].

Based on the current understanding on the precipitation process in the Mg-Zn alloy, the likely precipitation sequence is summarized in Fig. 13. In the usual notation for precipitation sequence, two precipitates that form consecutively during aging are connected by solid arrows, i.e., $A\rightarrow B$. This notation can lead to some confusion, since, other than thermodynamic stability, it can also be interpreted that B nucleates kinetically on the structure of A, where there usually exists a specific orientation relationship between A and B. To avoid the confusion in Fig. 13, arrows with solid lines are used if an orientation relationship exists between consecutively formed precipitates, while arrows with dashed lines are used if there is no clear orientation relationship.

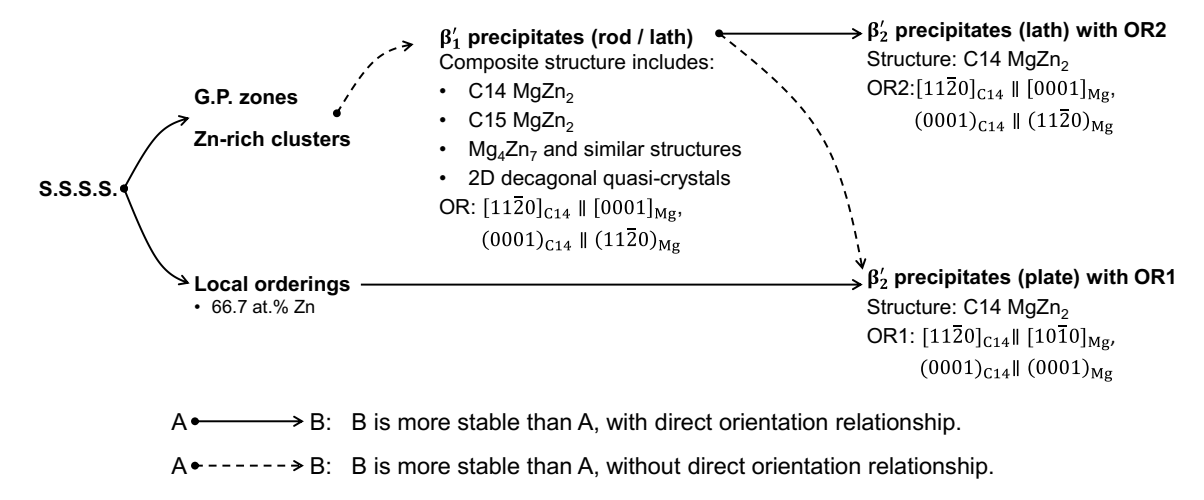


Fig. 13 The proposed precipitation sequence for supersaturated Mg-Zn solid solution during aging.

6. Conclusions

In the current work, the research status on crystal structures and stabilities of phases in Mg-Zn system is reviewed, and comprehensive first-principles calculations are performed to examine the

crystal structures and phase stability of precipitates and explore the remaining controversies. The main conclusions are summarized as the following.

- (1) Current calculations predict GP zones on $\{01\overline{1}0\}_{Mg}$, $\{2\overline{1}\overline{1}0\}_{Mg}$ and $\{0001\}_{Mg}$ planes, on which plate-like GP zones are reported in experiments to reside. The stabilities of the predicted GP zones at finite temperature are calculated and compared with experiments. Further, the effect of CSE on the stabilities of GP zones is explained in the case of GP sheets on $\{01\overline{1}0\}_{Mg}$ plane, i.e., the double-layered GP sheet in B19 family and the zigzagged one in D0₁₉ family.
- (2) The β_1' precipitate is made up of the MgZn₂ rhombic and the Mg₆Zn₇ elongated hexagonal units, which, with different arrangements, leads to domains of C14 and C15 MgZn₂, Mg₄Zn₇, 2D decagonal quasi-crystals and other decagonal approximants. The β_1' with more Mg₆Zn₇ elongated hexagonal units are less stable than ones with more MgZn₂ rhombic units building regions of C14 MgZn₂.
- (3) The β_2' (C14 MgZn₂) precipitates with OR1, i.e., $(0001)_{C14} \parallel (0001)_{Mg}$ and $[11\bar{2}0]_{C14} \parallel [10\bar{1}0]_{Mg}$ can form from the relaxation of the specific low energy ordering with 66.7 at. % Zn, while the β_2' with OR2, i.e., $[0001]_{C14} \parallel [11\bar{2}0]_{Mg}$ and $(11\bar{2}0)_{C14} \parallel (0001)_{Mg}$ forms by the same mechanism as that of the β_1' rod.

Acknowledgement

This work is supported by the U.S. National Science Foundation (NSF) DMREF grant CMMI-1921926, and the start-up funds from the University of Virginia. The authors acknowledge Advanced Research Computing Services at the University of Virginia for providing computational resources and technical support. This work also used the Extreme Science and Engineering Discovery Environment (XSEDE) resources, which is supported by NSF grant number ACI-1548562, via the Stampede2 supercomputer at the Texas Advanced Computing Center through allocation TG-MAT200016.

References

- [1] T.M. Pollock, Weight loss with magnesium alloys, *Science* (80-.). 328 (2010) 986–987.
- [2] M. Hakamada, T. Furuta, Y. Chino, Y. Chen, H. Kusuda, M. Mabuchi, Life cycle inventory study on magnesium alloy substitution in vehicles, *Energy*. 32 (2007) 1352– 1360.

- [3] J.F. Nie, Precipitation and hardening in magnesium alloys, *Metall. Mater. Trans. A.* 43A (2012) 3891–3939.
- [4] Y. Lu, A.R. Bradshaw, Y.L. Chiu, I.P. Jones, The role of β' precipitates in the biocorrosion performance of Mg-3Zn in simulated body fluid, *J. Alloys Compd.* 614 (2014) 345–352.
- [5] B. Zhou, J. Chen, H. Yan, W. Xia, B. Su, H. Guo, W. Zhu, To improve strength and bio-corrosion resistance of Mg-4Zn alloy via high strain rate rolling combined with double aging, *Mater. Lett.* 227 (2018) 301–304.
- [6] H. Pan, Y. Ren, H. Fu, H. Zhao, L. Wang, X. Meng, G. Qin, Recent developments in rare-earth free wrought magnesium alloys having high strength: A review, *J. Alloys Compd.* 663 (2016) 321–331.
- [7] H. Okamoto, Comment on Mg-Zn (Magnesium-Zinc), *J. Phase Equilibria*. 15 (1994) 129–130.
- [8] N.E.L. Saris, E. Mervaala, H. Karppanen, J.A. Khawaja, A. Lewenstam, Magnesium: An update on physiological, clinical and analytical aspects, *Clin. Chim. Acta.* 294 (2000) 1–26.
- [9] D. Zhu, I. Cockerill, Y. Su, Z. Zhang, J. Fu, K.W. Lee, J. Ma, C. Okpokwasili, L. Tang, Y. Zheng, Y.X. Qin, Y. Wang, Mechanical strength, biodegradation, and in vitro and in vivo biocompatibility of Zn biomaterials, *ACS Appl. Mater. Interfaces*. 11 (2019) 6809–6819.
- [10] P. Han, M. Tan, S. Zhang, W. Ji, J. Li, X. Zhang, C. Zhao, Y. Zheng, Y. Chai, Shape and site dependent in vivo degradation of Mg-Zn pins in rabbit femoral condyle, *Int. J. Mol. Sci.* 15 (2014) 2959–2970.
- [11] M. Gupta, N.M.L. Sharon, Introduction to Magnesium, *Magnesium, Magnes. Alloy. Magnes. Compos.* (2010) 1–12.
- [12] J.B. Clark, Transmission electron microscopy study of age hardening in a Mg-5 wt.% Zn alloy, *Acta Metall.* 13 (1965) 1281–1289.
- [13] J.S. Chun, J.G. Byrne, Precipitate strengthening mechanisms in magnesium zinc alloy single crystals, *J. Mater. Sci.* 4 (1969) 861–872.
- [14] G. Mima, Y. Tanaka, Main factors affecting the aging of magnesium- zinc alloys, *Trans. Japan Inst. Met.* 12 (1971) 76–81.
- [15] G. Mima, Y. Tanaka, Mechanism of Precipitation Hardening of Magnesium-Zinc Alloys,

- Trans. Japan Inst. Met. 12 (1971) 323-328.
- [16] G. Mima, Y. Tanaka, The aging characteristics of magnesium-4wt% zinc alloy, *Trans. Japan Inst. Met.* 12 (1971) 71–75.
- [17] T. Takahashi, Y. Kojima, K. Takanishi, Study of precipitates in an aged Mg-3. 6 wt% Zn alloy by an X-ray method, *Japan Inst. Light Met.* 23 (1973) 376–382.
- [18] L.Y. Wei, G.L. Dunlop, H. Westengen, Precipitation Hardening of Mg-Zn and Mg-Zn-RE Alloys, *Metall. Mater. Trans. A.* 26 (1995) 1705–1716.
- [19] S.Y. Komatsu, M. Ikeda, U. Mori, M. Abe, Increase in resistivity of Mg-Zn alloys by low temperature aging, *J. Japan Inst. Light Met.* 54 (2004) 131–136.
- [20] X. Gao, J.F. Nie, Characterization of strengthening precipitate phases in a Mg-Zn alloy, *Scr. Mater.* 56 (2007) 645–648.
- [21] J. Buha, Reduced temperature (22-100 °C) ageing of an Mg-Zn alloy, *Mater. Sci. Eng. A*. 492 (2008) 11–19.
- [22] R. Alizadeh, R. Mahmudi, T.G. Langdon, Creep mechanisms in an Mg-4Zn alloy in the as-cast and aged conditions, *Mater. Sci. Eng. A.* 564 (2013) 423–430.
- [23] M. Němec, V. Gärtnerová, M. Klementová, A. Jäger, Analysis of intermetallic particles in Mg-12 wt.%Zn binary alloy using transmission electron microscopy, *Mater. Charact.* 106 (2015) 428–436.
- [24] B. Langelier, G. Sha, A. Korinek, P. Donnadieu, S.P. Ringer, S. Esmaeili, The effects of microalloying on the precipitate microstructure at grain boundary regions in an Mg-Zn-based alloy, *Mater. Des.* 119 (2017) 290–296.
- [25] A. Bendo, T. Maeda, K. Matsuda, A. Lervik, R. Holmestad, C.D. Marioara, K. Nishimura, N. Nunomura, H. Toda, M. Yamaguchi, K. ichi Ikeda, T. Homma, Characterisation of structural similarities of precipitates in Mg–Zn and Al–Zn–Mg alloys systems, *Philos. Mag.* 99 (2019) 2619–2635.
- [26] S. Liu, G. Esteban-Manzanares, J. Llorca, First-principles analysis of precipitation in Mg-Zn alloys, *Phys. Rev. Mater.* 4 (2020) 93609.
- [27] W. Kohn, L.J. Sham, Self-Consistent Equations Including Exchange and Correlation Effects, *Phys. Rev.* 140 (1965) A1133.
- [28] P. Hohenberg, W. Kohn, Inhomogeneous Electron Gas, *Phys. Rev.* 136 (1964) 864.
- [29] A. van de Walle, Methods for first-principles alloy thermodynamics, *JOM*. 65 (2013)

- 1523-1532.
- [30] A. van de Walle, M. Asta, Self-driven lattice-model Monte Carlo simulations of alloy thermodynamic properties and phase diagrams, *Model. Simul. Mater. Sci. Eng.* 10 (2002) 521–538.
- [31] I. Higashi, N. Shiotani, M. Uda, T. Mizoguchi, H. Katoh, The crystal structure of Mg51Zn20, *J. Solid State Chem.* 36 (1981) 225–233.
- [32] M. Hida, Y. Matsui, The pseudocubic approximant Mg51Zn20 interpreted as a modulated crystal, *Philos. Mag. A.* 82 (2002) 831–839.
- [33] X. Gao, J.F. Nie, Structure and thermal stability of primary intermetallic particles in an Mg-Zn casting alloy, *Scr. Mater.* 57 (2007) 655–658.
- [34] L. Tarschisch, Röntgenographische Untersuchung der Verbindungen MgZn und MgZn5, *Zeitschrift Für Krist. Mater.* 86 (1933) 423–438.
- [35] R. Černý, G. Renaudin, The intermetallic compound Mg21Zn25, *Acta Crystallogr. C.* 58 (2002) 154–155.
- [36] Y. Khan, Dynamic temperature crystallization behaviour of amorphous and liquid Mg70Zn30 alloy, *J. Mater. Sci.* 24 (1989) 963–973.
- [37] J.B. Clark, F.N. Rhines, Central region of the Mg-Zn phase diagram, *JOM*. 9 (1957) 425–430.
- [38] L. Zhang, W. Wang, W. Hu, Z. Yang, H. Ye, Nanometer-sized domain structure in complex Mg21Zn25 formed by eutectoid phase transformation in a Mg-Zn alloy, *J. Alloys Compd.* 745 (2018) 319–330.
- [39] C.C. Kammerer, S. Behdad, L. Zhou, F. Betancor, M. Gonzalez, B. Boesl, Y.H. Sohn, Diffusion kinetics, mechanical properties, and crystallographic characterization of intermetallic compounds in the Mg-Zn binary system, *Intermetallics*. 67 (2015) 145–155.
- [40] K. Cenzual, E. Parthé, R.M. Waterstrat, Zr21Re25, a new rhombohedral structure type containing 12 Å-thick infinite MgZn2(Laves)-type columns, *Acta Crystallogr. C.* 42 (1986) 261–266.
- [41] J. Gallot, R. Graf, ., Comptes. Rendus. Acda. Sci. 262B (1966) 1219.
- [42] Y. Yarmolyuk, Crystal Structure of Mg4Zn7, Kristallografiya. 20 (1975) 538–542.
- [43] Q. -B Yang, K.H. Kuo, A new description of pentagonal Frank–Kasper phases and a possible structure model of the icosahedral quasicrystal, *Acta Crystallogr. A.* 43 (1987)

- 787–795.
- [44] Z. Yang, L. Zhang, M.F. Chisholm, X. Zhou, H. Ye, S.J. Pennycook, Precipitation of binary quasicrystals along dislocations, *Nat. Commun.* 9 (2018) 1–7.
- [45] A. Ovchinnikov, V. Smetana, A.V. Mudring, Metallic alloys at the edge of complexity: structural aspects, chemical bonding and physical properties, *J. Phys. Condens. Matter.* 32 (2020).
- [46] W.Z. Wang, X.Z. Zhou, Z.Q. Yang, Y. Qi, H.Q. Ye, A decagonal quasicrystal with rhombic and hexagonal tiles decorated with icosahedral structural units, *IUCrJ*. 7 (2020) 535–541.
- [47] E. Abe, A.P. Tsai, short communications Orthorhombic tau -Zn Mg Dy phase related to a Frank- Kasper type decagonal quasicrystal, *Acta Crystallogr. B.* (2000) 915–917.
- [48] M. Mihalkovič, J. Richmond-Decker, C.L. Henley, M. Oxborrow, Ab-initio tiling and atomic structure for decagonal ZnMgY quasicrystal, *Philos. Mag.* 94 (2014) 1529–1541.
- [49] J.B. Friauf, The crystal structure of magnesium di-zincide, *Phys. Rev.* 29 (1927) 34–40.
- [50] F. Laves, K. Lohberg, Die Kristallstruktur von intermet- allischen Verbindungen der Formel AB2 (The crystal structure of intermetallic compounds with formula AB2; in German), *Nachr Ges Wiss Go"ttingen, Math-Phys Kl IV, Neue Folge*. 1 (1934) 59–66.
- [51] F. Laves, H. Witte, Die Kristallstruktur des MgNi2 und seine Beziehungen zu den Typen des MgCu2 und MgZn2 (The crystal structure of MgNi2 and its relations to the MgCu2 and MgZn2 types; in German), *Met. Met. Met. Tech.* 14 (1935) 645–649.
- [52] F. Stein, A. Leineweber, Laves phases: a review of their functional and structural applications and an improved fundamental understanding of stability and properties, *J. Mater. Sci.* 56 (2021) 5321–5427.
- [53] T. Ohba, Y. Kitano, Y. Komura, The charge-density study of the Laves phases, MgZn2 and MgCu2, *Acta Crystallogr. C.* 40 (1984) 1–5.
- [54] W.J. Kim, S.I. Hong, K.H. Lee, Structural characterization of Laves-phase MgZn2 precipitated in Mg-Zn-Y alloy, *Met. Mater. Int.* 16 (2010) 171–174.
- [55] J.M. Rosalie, H. Somekawa, A. Singh, T. Mukai, Orientation relationships between icosahedral clusters in hexagonal MgZn2 and monoclinic Mg4Zn7 phases in Mg-Zn(-Y) alloys, *Philos. Mag.* 91 (2011) 2634–2644.
- [56] A. Jain, S.P. Ong, G. Hautier, W. Chen, W.D. Richards, S. Dacek, S. Cholia, D. Gunter,

- D. Skinner, G. Ceder, K.A. Persson, Commentary: The materials project: A materials genome approach to accelerating materials innovation, *APL Mater.* 1 (2013).
- [57] M. Andersson, M. de Boissieu, S. Brühne, C. Drescher, W. Assmus, S. Ohahshi, A.P. Tsai, M. Mihalkovič, M. Krajčí, Ö. Rapp, Electronic and structural properties of Lavesphase MgZn2 of varying chemical disorder, *Phys. Rev. B.* 82 (2010) 024202.
- [58] A. Singh, J.M. Rosalie, Lattice correspondence and growth structures of monoclinic mg4 zn7 phase growing on an icosahedral quasicrystal, *Crystals*. 8 (2018).
- [59] S. Samson, Ø. Ellefsen, O. Hassel, A. Kainulainen, A. Halonen, E. Pulkkinen, Die Kristallstruktur von Mg2Cu6Al5., *Acta Chem. Scand.* 3 (1949) 809–834.
- [60] H. Euchner, M. Mihalkovič, F. Gähler, M.R. Johnson, H. Schober, S. Rols, E. Suard, A. Bosak, S. Ohhashi, A.-P. Tsai, S. Lidin, C.P. Gomez, J. Custers, S. Paschen, M. de Boissieu, Anomalous vibrational dynamics in the Mg2Zn11 phase, *Phys. Rev. B*. 83 (2011) 144202.
- [61] Y. Murakami, K. Kawano, H. Tamura, Kyoto Univ. Memoirs of the Faculty of Eng., 1962.
- [62] T. Bhattacharjee, C.L. Mendis, K. Oh-ishi, T. Ohkubo, K. Hono, The effect of Ag and Ca additions on the age hardening response of Mg-Zn alloys, *Mater. Sci. Eng. A.* 575 (2013) 231–240.
- [63] D. Orlov, D. Pelliccia, X. Fang, L. Bourgeois, N. Kirby, A.Y. Nikulin, K. Ameyama, Y. Estrin, Particle evolution in Mg-Zn-Zr alloy processed by integrated extrusion and equal channel angular pressing: Evaluation by electron microscopy and synchrotron small-angle X-ray scattering, *Acta Mater.* 72 (2014) 110–124.
- [64] T. Bhattacharjee, C.L. Mendis, T.T. Sasaki, T. Ohkubo, K. Hono, Effect of Zr addition on the precipitation in Mg-Zn-based alloy, *Scr. Mater.* 67 (2012) 967–970.
- [65] T. Bhattacharjee, T. Nakata, T.T. Sasaki, S. Kamado, K. Hono, Effect of microalloyed Zr on the extruded microstructure of Mg-6.2Zn-based alloys, *Scr. Mater.* 90 (2014) 37–40.
- [66] L. Sturkey, J.B. Clark., Mechanism of age-hardening in magnesium-zinc alloys, *J. Inst. Met.* 88 (1959) 1960.
- [67] L.L. Rokhlin, A. Oreshkina, Research Into the Structure of a Metastable Phase Formed During the Breakdown of a Supersaturated Solution in Magnesium--Zinc Alloys, *Fiz. Met. Met.* 66 (1988) 12–17.

- [68] A. Singh, A.P. Tsai, Structural characteristics of β1'precipitates in Mg-Zn-based alloys, *Scr. Mater.* 57 (2007) 941–944.
- [69] D. Joubert, From ultrasoft pseudopotentials to the projector augmented-wave method, *Phys. Rev. B.* 59 (1999) 1758–1775.
- [70] J.P. Perdew, K. Burke, M. Ernzerhof, Generalized gradient approximation made simple, *Phys. Rev. Lett.* 77 (1996) 3865–3868.
- [71] G. Kresse, Efficient iterative schemes for ab initio total-energy calculations using a planewave basis set, *Phys. Rev. B.* 54 (1996) 11169–11186.
- [72] G. Kresse, J. Furthmüller, Efficiency of ab-initio total energy calculations for metals and semiconductors using a plane-wave basis set, *Comput. Mater. Sci.* 6 (1996) 15–50.
- [73] M. Methfessel, A.T. Paxton, High-precision sampling for Brillouin-zone integration in metals, *Phys. Rev. B.* 40 (1989) 3616–3621.
- [74] A. Van de Walle, M. Asta, G. Ceder, The alloy theoretic automated toolkit: A user guide, *CALPHAD*. 26 (2002) 539–553.
- [75] P.E. Blöchl, O. Jepsen, O.K. Andersen, Improved tetrahedron method for Brillouin-zone integrations, *Phys. Rev. B.* 49 (1994) 16223–16233.
- [76] J.M. Sanchez, F. Ducastelle, D. Gratias, Generalized cluster description of multicomponent systems, *Physica A*. 128 (1984) 334–350.
- [77] D.B. Laks, L.G. Ferreira, S. Froyen, A. Zunger, Efficie cluster expansion for substitutional systems, *Phys. Rev. B.* 46 (1992) 12587.
- [78] A. van de Walle, Multicomponent multisublattice alloys, nonconfigurational entropy and other additions to the Alloy Theoretic Automated Toolkit, *CALPHAD*. 33 (2009) 266–278.
- [79] A. van de Walle, G. Ceder, Automating first-principles phase diagram calculations, *J. Phase Equilibria*. 23 (2002) 348–359.
- [80] A.H. Nguyen, C.W. Rosenbrock, C.S. Reese, G.L.W. Hart, Robustness of the cluster expansion: Assessing the roles of relaxation and numerical error, *Phys. Rev. B.* 96 (2017) 1–11.
- [81] K. Wang, D. Cheng, C. Fu, B. Zhou, First-principles investigation of the phase stability and early stages of precipitation in Mg-Sn alloys, *Phys. Rev. Mater.* 013606 (2020) 1–13.
- [82] A.R. Natarajan, J.C. Thomas, B. Puchala, A. Van Der Ven, Symmetry-adapted order

- parameters and free energies for solids undergoing order-disorder phase transitions, *Phys. Rev. B.* 96 (2017) 1–13.
- [83] B. Sadigh, P. Erhart, A. Stukowski, A. Caro, E. Martinez, L. Zepeda-Ruiz, Scalable parallel Monte Carlo algorithm for atomistic simulations of precipitation in alloys, *Phys. Rev. B Condens. Matter Mater. Phys.* 85 (2012) 184203.
- [84] C.N. Varney, G.L.W. Hart, C. Wolverton, A Coherency Strain Model for Hexagonal-Close-Packed Alloys, *TMS Lett.* 1 (2005) 35–36.
- [85] A. Issa, J.E. Saal, C. Wolverton, Physical factors controlling the observed high-strength precipitate morphology in Mg-rare earth alloys, *Acta Mater.* 65 (2014) 240–250.
- [86] K. Wang, D. Cheng, B. Zhou, Generalization of the mixed space cluster expansion method for arbitrary lattices, submitted to npj Computational Materials, (2022).
- [87] V. Ozoliņš, C. Wolverton, A. Zunger, Effects of anharmonic strain on the phase stability of epitaxial films and superlattices: Applications to noble metals, *Phys. Rev. B.* 57 (1998) 4816–4828.
- [88] S. Shang, Y. Wang, Z.K. Liu, First-principles elastic constants of α- And θ- Al2O3, *Appl. Phys. Lett.* 90 (2007) 1–4.
- [89] M. De Jong, W. Chen, T. Angsten, A. Jain, R. Notestine, A. Gamst, M. Sluiter, C.K. Ande, S. Van Der Zwaag, J.J. Plata, C. Toher, S. Curtarolo, G. Ceder, K.A. Persson, M. Asta, Charting the complete elastic properties of inorganic crystalline compounds, *Sci. Data.* 2 (2015) 1–13.
- [90] Robert E Newham, Properties of Materials Anisotropy, Symmetry, Structure, Oxford University Press, 2005.
- [91] M. Hellenbrandt, The inorganic crystal structure database (ICSD) Present and future, *Crystallogr. Rev.* 10 (2004) 17–22.
- [92] J.E. Saal, S. Kirklin, M. Aykol, B. Meredig, C. Wolverton, Materials design and discovery with high-throughput density functional theory: The open quantum materials database (OQMD), *JOM*. 65 (2013) 1501–1509.
- [93] S. Wasiur-Rahman, M. Medraj, Critical assessment and thermodynamic modeling of the binary Mg-Zn, Ca-Zn and ternary Mg-Ca-Zn systems, *Intermetallics*. 17 (2009) 847–864.
- [94] N.C. Verissimo, C. Brito, C.R. Afonso, J.E. Spinelli, N. Cheung, A. Garcia, Microstructure characterization of a directionally solidified Mg-12wt.%Zn alloy:

- Equiaxed dendrites, eutectic mixture and type/ morphology of intermetallics, *Mater*. *Chem. Phys.* 204 (2018) 105–131.
- [95] C. Ravi, C. Wolverton, First-principles study of crystal structure and stability of Al-Mg-Si-(Cu) precipitates, *Acta Mater.* 52 (2004) 4213–4227.
- [96] D. Wang, M. Amsler, V.I. Hegde, J.E. Saal, A. Issa, B.C. Zhou, X. Zeng, C. Wolverton, Crystal structure, energetics, and phase stability of strengthening precipitates in Mg alloys: A first-principles study, *Acta Mater.* 158 (2018) 65–78.
- [97] R. Agarwal, S.G. Fries, H.L. Lukas, G. Petzow, E. Sommer, T.G. Chart, G. Effenberg, Assessment of the Mg-Zn System, *Int. J. Mater. Res.* 83 (1992) 216–223.
- [98] M. Mihalkovic, M. Widom, Alloy database, *Http://Alloy.Phys.Cmu.Edu/*. (2011).
- [99] A. Schneider, H. Klotz, J. Stendel, G. Strauss, Zur Thermochemie von Legierungen, *Pure Appl. Chem.* 2 (1961) 13–16.
- [100] L.W. McKeehan, ., Z. Krist. Tl. A. 91 (1935) 501–503.
- [101] R. King, O. Kleppa, A thermochemical study of some selected laves phases, *Acta Metall*. 12 (1964) 87–97.
- [102] M. Morishita, H. Yamamoto, S. Shikada, M. Kusumoto, Y. Matsumoto, Thermodynamics of the formation of magnesium-zinc intermetallic compounds in the temperature range from absolute zero to high temperature, *Acta Mater.* 54 (2006) 3151–3159.
- [103] A. Berche, C. Drescher, J. Rogez, M.C. Record, S. Brühne, W. Assmus, Thermodynamic measurements in the Mg-Zn system, *J. Alloys Compd.* 503 (2010) 44–49.
- [104] V.W. Blitz, G. Hohorst, Die Bildungswärmen der Verbindungen von metallischem Magnesium mit metallischem Zink, Cadmium, Aluminium und Calcium, (1922) 1–21.
- [105] Y. Komura, K. Tokunaga, Structural studies of stacking variants in Mg-base Friauf–Laves phases, *Acta Crystallogr. B.* 36 (1980) 1548–1554.
- [106] A.R. Natarajan, E.L.S. Solomon, B. Puchala, E.A. Marquis, A. Van Der Ven, On the early stages of precipitation in dilute Mg-Nd alloys, *Acta Mater.* 108 (2016) 367–379.
- [107] D. Cheng, E.R. Hoglund, K. Wang, J.M. Howe, S.R. Agnew, B. Zhou, Atomic structures of ordered monolayer GP zones in Mg-Zn-X (X = Ca, Nd) systems, *Scr. Mater.* 216 (2022) 114744.
- [108] V. Vaithyanathan, C. Wolverton, L.Q. Chen, Multiscale modeling of θ' precipitation in Al-Cu binary alloys, *Acta Mater*. 52 (2004) 2973–2987.

- [109] V. Ozoliņš, C. Wolverton, A. Zunger, Strain-induced change in the elastically soft direction of epitaxially grown face-centered-cubic metals, *Appl. Phys. Lett.* 72 (1998) 427–429.
- [110] C. Wolverton, First-principles theory of 250,000-atom coherent alloy microstructure, *Model. Simul. Mater. Sci. Eng.* 8 (2000) 323–333.
- [111] J.M. Rosalie, H. Somekawa, A. Singh, T. Mukai, Structural relationships among MgZn2 and Mg4Zn 7 phases and transition structures in Mg-Zn-Y alloys, *Philos. Mag.* 90 (2010) 3355–3374.
- [112] P.J. Steinhardt, H.C. Jeong, A simpler approach to Penrose tiling with implications for quasicrystal formation, *Nature*. 382 (1996) 431–433.
- [113] A.S. Keys, S.C. Glotzer, How do quasicrystals grow?, Phys. Rev. Lett. 99 (2007) 1–4.
- [114] A.R. Natarajan, A. Van Der Ven, Connecting the Simpler Structures to Topologically Close-Packed Phases, *Phys. Rev. Lett.* 121 (2018) 255701.